TAMPEREEN TEKNILLINEN YLIOPISTO
TAMPERE UNIVERSITY OF TECHNOLOGY

Iiro Hiltunen

Tools for Cryogenic Design of Superconducting Induction Heater

Julkaisu 923 • Publication 923

Tampere 2010

Tampereen teknillinen yliopisto. Julkaisu 923
Tampere University of Technology. Publication 923

Iiro Hiltunen

Tools for Cryogenic Design of Superconducting Induction Heater

Thesis for the degree of Doctor of Science in Technology to be presented with due permission for public examination and criticism in Rakennustalo Building, Auditorium RG202, at Tampere University of Technology, on the 19th of November 2010, at 12 noon.

Tampereen teknillinen yliopisto - Tampere University of Technology
Tampere 2010

ISBN 978-952-15-2455-4 (printed)
ISBN 978-952-15-2470-7 (PDF)
ISSN 1459-2045

Abstract

The design of cryogenic systems requires knowledge about many material parameters to accurately simulate the system before the construction. This thesis presents the cryogenic design of a superconducting induction heater in an Aluheat project and important tools and simulation models needed whilst designing this system. These tools and models provide better understanding about the material properties as well as about the characterization of short samples and coils to improve existing simulation models.

First, I present the physical background of concepts used in the thesis. To evaluate the coil stability, and to simulate quench, the transverse thermal conductivity of a MgB_2 coil was measured and simulated. Furthermore, the viability of several solders for small scale HTS current lead construction was shown and their performance compared against commercial current lead designs. Next, I studied the short sample and coil characterization and stability by means of voltage (V) current (I) characteristics. A method to improve the $V(I)$ characteristics of the conduction cooled short samples was presented and tested for two superconducting tapes. Simulations of charging characteristics of the coil were also studied.

Finally, the design of a superconducting induction heater with improved efficiency is shown, and some issues faced during the project explained.

Preface

This thesis has been carried out between 2004 and 2010 at Electromagnetics at Department of Electronics at Tampere University of Technology. The thesis concludes my study about superconducting induction heaters, started as a M.Sc. thesis in 2003. During these years, I have learned a lot about superconductivity, modeling and cryogenics. Beyond the scientific study, countless hours in laboratory have taught me something about 3d-modeling, machining, welding, soldering, vacuum equipment, material properties and electronics. For everything, I would like to thank the head of our department, Professor Lauri Kettunen for providing admirable atmosphere and excellent working facilities.

Second, I wish to express my deepest gratitude to my main instructor Dr. Jorma Lehtonen for shoving me into a trail of scientific research, giving me suggestions now and then, and keeping me sane along the way. I am also grateful to Risto Mikkonen, my supervisor, who employed me in the first place and organized funding for my research. His leadership was always exceptional.

I thank Aki Korpela for proof-reading the thesis, inspiring me to exercise more and lending an ear when needed. Antti Stenvall, who was outstanding company at conference trips and offered essential assistance regarding Matlab, Latex and simulation models. Sincere thanks belong also to my latest roommate in work, Joonas Järvelä for his entertaining stories and for his invaluable help in chores at our laboratory especially during the assembly of the induction heater. I could not have done it alone.

Special thanks goes to Hannu Nieminen and Pekka Nousiainen who got me convinced there is a way to construct these absurd looking parts I designed with slight modifications. I thank also all the people in Protopaja workshop for constructing many parts for Aluheat.

All in all, a number of fellow students and colleagues, although many of them have left the department, have contributed to social environment and inspiring work - thanks.

Finally, I would like to thank my parents for the advices and guidelines in life which have carried me this far. I will keep up the good work!

This work was funded and materially supported by European Union (contract ALUHEAT-013683) and Department of Electronics at Tampere University of Technology.

Knowledge rests not upon truth alone, but upon error also.
-Carl Gustav Jung

In Tampere, 15 October, 2010

Iiro Hiltunen

List of publications

Publication I
Hiltunen I, Korpela A, Lehtonen J and Mikkonen R
"Influence of current ramp rate on voltage current measurement of a conduction-cooled HTS magnet"
Physica C. **468** 903, 2007
doi:10.1016/j.physc.2008.03.003

Publication II
Hiltunen I, Korpela A, Laine H, Lehtonen J, Lyly M and Mikkonen R
"Measured Performance of Different Solders in Bi2223/Ag Current Leads"
IEEE Trans. Appl. Supercond. **18** 1427, 2008
doi:10.1109/TASC.2008.920618

Publication III
Hiltunen I, Stenvall A, Korpela A, Lehtonen J, Mikkonen R, Runde M, Magnusson N and Kalkowski G
"Cryogenic Design of the Aluheat Project"
Advances in Cryogenic Engineering **53** 1015, 2008
doi:10.1063/1.2908448

Publication IV
Hiltunen I, Järvelä, Lehtonen J, Mikkonen R, Stenvall A and Viljamaa J
"Transverse Thermal Conductivity in an Epoxy Impregnated MgB_2 Coil"
IEEE Trans. Appl. Supercond. **19** 2407, 2009
doi:10.1109/TASC.2009.2018045

Publication V
Hiltunen I, Lehtonen J, Mikkonen R and Stenvall A
"Method to determine critical current of poorly cooled short sample"
Physica C. **469** 1987, 2009
doi:10.1016/j.physc.2009.07.007

Publication VI
Hiltunen I, Lehtonen J, Stenvall A and Mikkonen R
"Influence of Self-heating on Measured n-value"
IEEE Trans. Appl. Supercond. **20** 1597-1600, 2010
doi:10.1109/TASC.2010.2042156

Publication VII
Sætre F, Hiltunen I, Järvelä J, Magnusson N, Runde M, Bjerkli J and Engebrethsen E
"Winding, cooling and testing of a 5 H superconducting MgB_2 coil for an induction heater"
submitted to publication

Contents

Lists of symbols and abbreviations

a	Half of the tape thickness
A	Cross-sectional area
B	Magnetic flux
B_1	Magnetic flux density at a current of 1 A
B_c	Critical magnetic flux density
B_c1	Lower critical magnetic flux density
B_c2	Upper critical magnetic flux density
B_e	External magnetic field density
B_mag	Magnetic flux density inside the sample
B_p	Penetration magnetic flux density
C_p	Specific heat
E	Electric field
E_c	Electric field criterion
f	Frequency
F_St	Force affecting cryostat without current
F_Rot	Force affecting cryostat with current
I	Current
I_c	Critical current
I_c0	Corrected critical current
I_c1	Critical current at ascending ramp
I_c2	Critical current at descending ramp
I_r	Current ramp rate
I_s	Thermal runaway current
J	Current density
J_c	Critical current density
k	Multiplier
K_ed	Geometry dependent factor
l	Length
L	Length of the current lead
M	Magnetization

n	Index number of superconductor
n_{d}	Differential n-value
N_{l}	Number of multi-insulation layers
p	Volumetric heat generation power
p_{mag}	Volumetric magnetization loss
p_{self}	Volumetric self field loss
P_{a}	Radiated heat load
P_{ed}	Eddy current losses
P_{h}	Power of the heater
P_{o}	Ohmic heat loss
P_{t}	Total heat leak
P_{s}	Heat flux along coil support
P_{r}	Radiated heat flux from the outer crystat wall
P_{l}	Heat flux along current leads including Ohmic losses
$P_{\mathrm{r,rs}}$	Heat radiated to radiation shield from the outer wall
P_{ave}	Average loss power
q	Heat flux density
Q_1	Heating energy during the ramp from zero current to I_{c1}
Q_2	Heating energy during the ramp from I_{c1} to I_{c2}
S	Area of filamentary region
t	Time
T	Temperature
T_0	Initial sample temperature
T_1	Sample temperature at I_{c1}
T_2	Sample temperature at I_{c2}
T_{a}	Temperature at one side of the contact
T_{b}	Temperature at other side of the contact
T_{c}	Temperature at the lower end of the lead
T_{cr}	Critical temperature
T_{w}	Temperature at the upper end of the lead
U	Total heat transfer coefficient
U_{b}	Heat transfer coefficient on material boundary
V	Voltage
V_{c}	Threshold voltage
x	Unknown constant
X_1	Direction parallel to the broad tape face
X_2	Direction perpendicural to the broad tape face
X_3	Direction along the tape
y	Unknown constant
α	Aspect ratio of the conductor
β	Volumetric fraction of the superconductor in the magnet

ΔT	Temperature difference
γ	Electrical conductivity in per cent of International Annealed Copper Standard
λ	Thermal conductivity
λ_{eff}	Transverse effective thermal conductivity
$\lambda_{85\mathrm{c}}$	Thermal conductivity at 85 °C
μ_0	Permeability of vacuum
Ω	Volume
ϕ	Field orientation
Φ_0	Magnetic flux quantum
ρ_{Cu}	Electrical resistivity of copper
σ_{u}	Tensile strength
AC	Alternating current
Aluheat	Project for building High efficiency aluminium billet induction heater
ASC	American superconductor corporation
BCS	Theory formulated by Bardeen, Cooper and Schrieffen
Bi-2223	Bismuth based high temperature superconductor
Bi-2212	Bismuth based high temperature superconductor
BSCCO	Bismuth based high temperature superconductors
Cernox	One type of temperature sensor
DC	Direct current
FEM	Finite element method
HTS	High Temperature Superconductors
G-10	Certain type of epoxy
G-11	Another type of epoxy
IACS	International annealed copper standard
LTS	Low temperature superconductor
MgB_2	Magnessium Diboride
MRI	Magnet resonance imaging
NMR	Nuclear magnetic resonance
n-value	Index value of superconductor
OFHC	Oxygen free high conductivity
OFHP	Oxygen free high purity
PIT	Powder in tube
RRR	Residual resistance ratio
SINTEF	Energy research center located in Norway
SMES	Superconducting energy storage
Stycast	Epoxy type
TUT	Tampere university of technology

YBCO Yttrium barium copper oxide

Chapter 1

Introduction

Superconductors, materials which have no resistance, are one of the great discoveries of the last century. For a superconducting state to exist, three parameters, magnetic flux density, temperature and current density, must remain under certain critical values. In a typical metal in the normal state, traveling electrons collide with the atoms leading to energy losses characterized as resistivity of the material, but in the superconducting state electrons can travel through the material freely without heat losses. Superconducting loops have been shown to carry electrical currents for numerous years with no measurable losses. The loss of resistance is caused by a complicated quantum mechanical phenomenon, which can be described with weak linking electron pairs. These Cooper pairs are constantly forming, breaking and reforming offering small amounts of electrons a freeway through the atomic lattice.

Over the years superconductors have surpassed their expected limits of performance and still continue to evolve. After niobium superconductors, new bismuth based high temperature superconductors were discovered in 1986. MgB_2 was discovered in 2001, iron-based superconductors in 2008 [21] and now, the newest addition are hydrocarbon superconductors found in 2010 [65]. Theories explaining the superconductivity are constantly under review, and scientists are still not unanimous with how superconductors work. The BCS theory, formulated by Bardeen, Cooper and Schrieffer, is the leading theory explaining

low-temperature superconductivity. However, it is not capable of explaining the high-temperature superconducting materials. Moreover, the BCS theory can not explain superconductivity in MgB_2 or in the new iron-based superconductors.

1.1 Motivation

Superconductors improve conventional applications by creating more compact, more powerful and more efficient systems as well as enable entirely new applications. In conventional applications, superconductors are mainly used to reduce electrical losses to improve efficiency. As maximum attainable field increases with improving conductors, engineers begin to offer some attractive alternatives for conventional methods in cables, transformers, high field magnets etc. This thesis focuses on cryostat and coil design as well as manufacturing of a superconducting induction heater used in the metal industry. In addition to a MgB_2 tape, as a potential competitor in induction heaters, a BSCCO tape is studied as well [50]. Thesis also includes some issues needed to be addressed during the design process which widened the scope of the study. The aim of the work is to present the cryogenic design of Aluheat project and to develop tools for coil and current lead design in such systems. Methods to improve the determination of voltage current characteristics needed in the design were also studied.

1.2 Structure of the thesis

The second chapter clarifies the work by introducing some physical background and the concept of the Aluheat induction heater. The third and fourth chapter are about simulating and minimizing losses in superconducting systems. Transverse thermal conductivity in epoxy impregnated magnesium diboride coils is measured and simulated to estimate the stability of the coil during the quench in the chapter three.

The chapter four deals with measuring contact resistances in different solders in order to reduce the resistance losses in current leads. Current leads are one of the main components contributing to the heat losses in the cryogenic system. The fifth and sixth chapter deal with coil characterization and stability. In the chapter five, challenges in short sample characterization are analyzed, and in chapter six a charging characteristics of a BSCCO coil are simulated. The seventh chapter introduces the cryogenic design of Aluheat and some results of the cool down.

1.3 Contributions

I, the author, have written all of the papers and made all of the simulations as well as measurements presented in the papers with the following exceptions. J. Lehtonen supervised the papers and gave some valuable insights for the thesis, A. Stenvall helped me with some of the simulation issues, and A. Korpela helped in proof reading some of the papers. R. Mikkonen is the head of our research group. Furthermore, in Publication II, H. Laine and M. Lyly made part of the thermal contact measurements. In Publication III, M. Runde and N. Magnusson wrote the section concerning the coil design and G. Kalkowski provided the section concerning the rotation of the billet. In Publication IV, the coil used was originally wound by J. Järvelä and J. Viljamaa for other testing purposes. Publication VII was organized by SINTEF/NTNU through F. Sætre, M. Runde, N. Magnusson, J. Bjerkli, and E. Engebrethsen, who designed the coil and developed the winding process, as well as performed the actual winding and assembly of the coil. J. Järvelä helped with preliminary testing of the system in Tampere.

Chapter 2

Physical background

This chapter introduces the basics of superconductivity needed to understand the subsequent chapters. First, basic definitions, superconductor characterization and AC-losses are explained. The remainder of the chapter focuses on superconducting materials properties used in the thesis and superconducting applications. Since this thesis focuses mainly on superconducting applications such as induction heater, microscopical analysis of the tapes and materials as well as theories are kept to a minimum.

2.1 Superconductivity

Superconductivity cannot be explained solely with perfect conductivity, but is characterized by a phenomenon called Meissner effect where weak external magnetic field B_{e} is penetrated only to a very small distance called the London penetration depth when the sample is cooled below the critical temperature T_{cr}. Superconductors can be divided into Type I and Type II superconductors (Fig. 2.1) according to their behavior in magnetic field. Most Type I conductors are pure elements like Al, Hg, Sn etc. When the external magnetic field B_{e} is below the critical magnetic flux density value B_{c}, the magnetic flux density inside the sample B_{mag} is zero due to the Meissner effect. When B_{e} exceeds B_{c}, flux expulsion no longer takes place, and the superconductivity is lost.

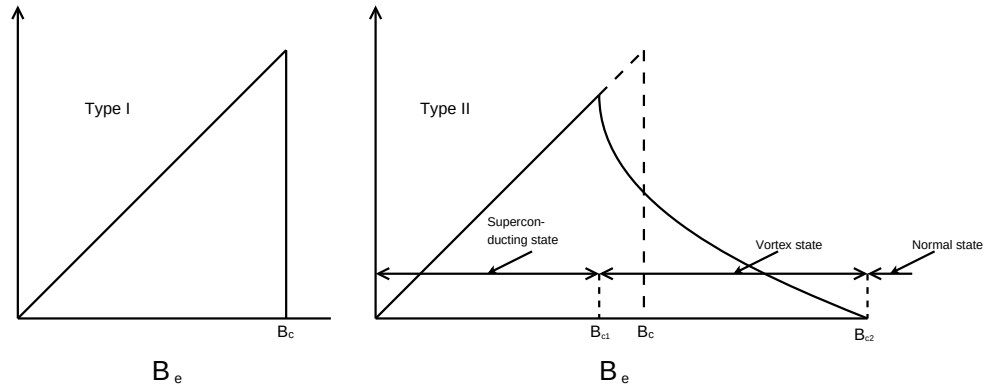

Figure 2.1: Magnetization curves for type I and type II superconductors.

A type-II superconductor is characterized that there are two critical fields (flux densities), B_{c1} and B_{c2}. For $B_e < B_{c1}$, the situation is similar like in the case of type-I superconductivity. For $B_e > B_{c1}$, the external magnetic field penetrates in the form of magnetic flux vortices which have a well defined size and carry a magnetic flux quantum Φ_0. The name mixed state comes from the fact that the centre of a flux vortex is no longer superconducting but in the normal state. Then, one has superconducting and non-superconducting regions in the material. By increasing the external field, the density of flux vortices increases until the full cross section is filled with them. In this situation, B_{c2} has been reached and there is no superconducting region left: the whole material is now normal conducting. It is also important to note that B_{c2} is much higher than B_{c1} allowing the generation of very high magnetic fields, which is not possible with type-I superconductors.

The relation between B_{mag}, B_e and the magnetization M can be formulated as

$$B_{mag} = B_e + M. \tag{2.1}$$

In the Meissner state, flux is completely expulsed, and thus, $B_{mag} = 0$ and $B_e = -M$. Values of B_{c1} and B_{c2} are typically around 0.1 T and 10-100 T, respectively. Table 2.1 shows typical values of T_{cr} and B_{c2} for some superconducting materials. [67]

Table 2.1: Typical values of T_{cr} and B_{c2} for some superconducting materials [42].

Material	T_{cr}	B_{c2}
Bi-2223	108	>100 T (4 K)
MgB_2	39	15 T (4 K)

The critical current of a superconductor is in addition to T_{cr} and the critical field the third parameter which limits the superconducting state. The critical current in a type-II superconductor is reached when the Lorentz force between the current and the flux vortices causes the vortices to move. In other words, the Lorentz force exceeds the pinning force of vortices. Because pinning forces depend of all kind of defects in the superconductor, the critical current is not material specific like T_{cr} and B_c.

2.2 Current-voltage characteristics and AC losses

Especially in HTS or MgB_2 superconductors, the transition from the superconducting to the normal state does not happen abruptly when the current is increased. Therefore, the design of superconducting applications should be based on voltage-current $V(I)$ characteristics instead of the critical current.

In a $V(I)$ measurement, a slowly increasing current ramp is fed to a specimen while the voltage between two voltage taps is measured. Critical current I_c is obtained, when the voltage reaches a certain threshold value V_c. Typically used the V_c values for superconducting leads are 0.1 μV/cm or 1 μV/cm. Afterwards, power-law

$$V = V_c \left(\frac{I}{I_c} \right)^n . \tag{2.2}$$

can be fitted into the measured $V(I)$-curve to accurately specify the critical current and the steepness of the transition represented by index value n. For accurate data, the temperature of the sample must be kept constant enough to prevent the deformation of the $V(I)$-curve. Also, B_e is assumed constant during the measurement. An example of the $V(I)$-curve is shown in Fig. 2.2.

When n-value is finite, resistive losses arise even at subcritical currents. Even with infinite n-value, whenever the changing magnetic field penetrates the superconductor, an electric field is created, and thereby, AC losses are generated. General equation for losses can be formulated as

$$P_{\text{ave}} = f \oint_{1/\text{f}} \frac{1}{\Omega} \int_{\Omega} E \cdot J d\Omega dT \tag{2.3}$$

where P_{ave} is the average loss power during a cycle, f the frequency, E electrical field, J current density and Ω the volume.

These losses depend on many parameters such as dimensions, external field amplitude, orientation and frequency, as well as, amplitude and frequency of transport current, pinning properties and filamentary structure. While there are many different loss mechanisms at play, here we focus on losses that originate at large amplitudes and low frequencies in the critical state. Losses that originate in a superconductor under changing B_{e} are called magnetiza-

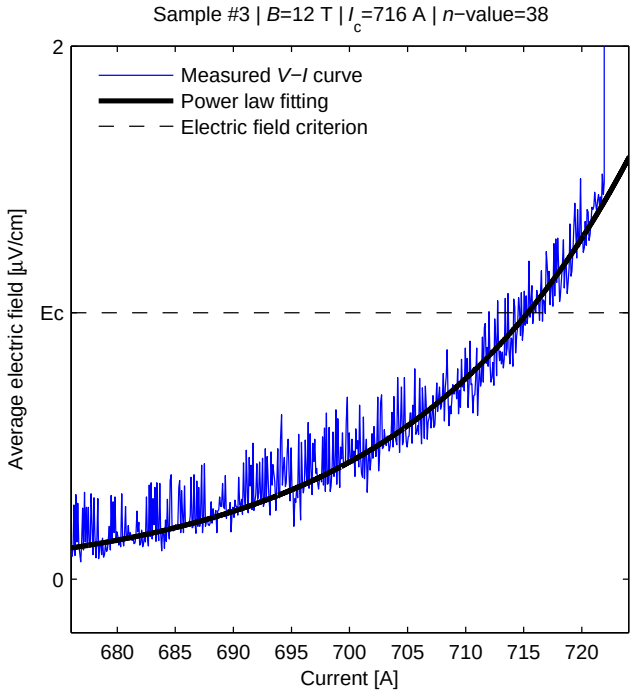

Figure 2.2: Example of measured $V(I)$-curve at vicinity of critical current.

tion losses while self-field losses develop due to the flowing AC current in the sample.

Losses can be reduced by dividing the superconductors into fine filaments surrounded by metallic matrix. Metal also carries heat away to improve stability and helps to spread the current between the filaments. However, procedure introduces additional eddy current losses in the copper matrix. Magnetization losses can also be reduced by twisting the wire which helps to untrap the flux.

2.3 Superconducting materials

Some superconducting materials like LTS are already widely used in industrial applications such as magnet resonance imaging MRI, whereas other materials like HTS is slowly emerging. New superconductors like MgB_2, are exposed to intensive study to make them feasible at present as well as at brand new applications. This section presents the materials used in this study.

Among the most studied HTS materials are $(Bi,Pb)_2Sr_2Ca_2Cu_3O_{10+x}$ (Bi-2223) and $Bi_2Sr_2Ca_1Cu_2O_{8+x}$ (Bi-2212). The former has the critical temperature of 108 K while the latter has T_c of 95 K. Both materials are used in insert magnets and in electrical power systems. Ceramic BSCCO is both brittle and fragile, and thus, BSCCO wires are usually produced as composite tapes manufactured using the powder in tube (PIT) method. For chemical and mechanical reasons, BSCCO filaments are surrounded with silver or silver alloy. Furthermore, a stainless steel jacket can be used on both sides of the tape for reinforcement. Typically tape contains tens of filaments that have a cross section around 200 μm^2.

MgB_2 is a very promising candidate for many applications at temperatures ranging from 4 K to 30 K. After an intensive nine year study, the feasibility of MgB_2 has already been demonstrated for MRI systems, induction heating, fault current limiters and transformers. MgB_2 is manufactured out of cheap and common materials which makes it an attractive competitor among other

materials. Depending on the application, MgB_2 can be formed as wires or tapes. Currently, MgB_2 conductors are manufactured by three companies, Hitachi, Hyper Tech research and Columbus Superconductors.

In this study we used two superconducting tapes. Bi-2223/Ag used in the study was composite tape, manufactured by American Superconductor Corporation (ASC). Later this will be referred as BSCCO tape. MgB_2/Ni/Fe/Cu tape used in the study was provided by Columbus Superconductors and was fabricated with the *exsitu* PIT method. Later this will be referred as MgB_2 tape. Table 2.2 shows the properties of the tapes used in this thesis. The cross-section of both conductors are shown in Fig. 2.3.

2.4 Cryogenics

Cryogenics and cooling are closely related to superconductors which operate only in cold temperatures. As a result of pioneering work, low-temperature engineering has taken major leaps over the years. In addition to the popular liquid cryogens like helium and nitrogen, the improvement of efficiencies of

Table 2.2: Properties of used superconducting tapes [1, 39, 57, 58]

Workname	Tape	Width	Thickness	Filaments	T_{cr}
BSCCO tape	Bi-2223/Ag	4.1 mm	0.3 mm	37	108
MgB_2 tape	MgB2/Ni/Fe/Cu	3.6 mm	0.65 mm	14	39

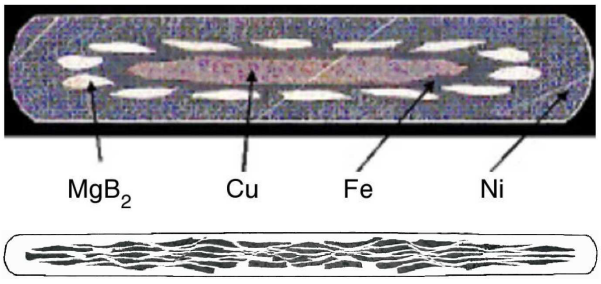

Figure 2.3: Cross-section of MgB_2/Ni/Fe/Cu conductor (upper) and Bi-2223/Ag conductor (lower) used.

small scale cryocoolers has been swift and opened potential for new applications. Nowadays, cryogens can be replaced using cryocoolers. It is also possible to construct condensing systems in which the evaporating cryogen is liquefied using a cryocooler and circulated back into system.

Mechanical engineering is quite different at cryogenic temperatures. Many materials and fluids behave completely differently compared to those of our ordinary experience. Liquids have extremely low heats of vaporization, specific heats are unexpectedly low, mechanical properties of materials are anomalous and shrinking materials may create huge forces during the cool down. Basic idea of good cryogenic design is to, as efficiently as possible, minimize the heat leak from outside and extract the losses from inside, thus, creating a stable atmosphere for superconductors. Good cryogenic design also protects the systems in case of a quench or other unwanted scenarios [15].

2.5 Concept of Aluheat

Superconductivity is already utilized in many applications. Superconducting coils are used in MRI, NMR, particle accelerators, magnetic separation and in mass spectrometers. Present applications in electronics include microwave filters, digital circuits and magnetometers. In future, already much studied applications such as Maglev trains, fault current limiters, power storage systems, transformers and superconducting cables and motors, might be ready for commercialization. Evolution of superconductors also opens markets for new applications including a superconducting induction heater.

This thesis concentrates on project High Efficiency Aluminium Billet Induction Heater, short Aluheat. In an induction heater the changing magnetic field induces eddy currents that heat up a billet. Conventional induction heaters use alternating current in a copper coil to create the changing magnetic field. Unfortunately, significant ohmic losses are generated, and the total efficiency decreases drastically. The basic idea of the superconducting induc-

tion heater is to improve the total efficiency. This cannot be done by simply feeding a superconducting coil with AC current due to the AC losses of a superconductor. However, heating can be attained if a billet is rotated in an inhomogeneous DC magnetic field created with a superconducting coil. Both concepts are presented in the Fig. 2.4.

Small demonstration devices in which a superconducting coil is supplied with DC current have already been introduced by SINTEF in Norway [51]. Futhermore, Zenergy power has built commercial induction heater using BSCCO tape [50]. Since superconductors are lossless at the direct currents, the input power is needed only to cool down the superconducting coil and rotate the billet. Therefore, the superconducting induction heater is more efficient compared to the conventional one when heating low resistivity materials like copper or aluminum. Efficiency in conventional induction heaters is only around 55% whereas with superconductivity the efficiency can be increased to around 90% [27, 51]. This is substantial increase and since the total power of heaters usually exceeds 1 MW significant cost savings can be achieved.

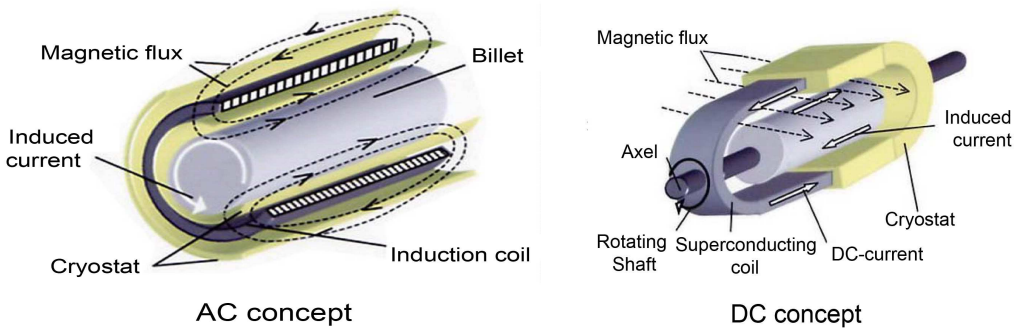

Figure 2.4: Alternating current induction heater (left) and direct current induction heater (right) [52].

Chapter 3

Transverse thermal conductivity

While designing superconducting systems, cryogenics and coil design require many parameters and data which is often unavailable. Measurements and simulations for these parameters are needed to backup the design. In this chapter, transverse thermal conductivity is measured and simulated from a small piece of MgB_2 coil. The thermal conductivity data is needed to ensure the homogeneous cooling of the coil and its thermal stability after the quench. That is, the underlying aim is to guarantee the safe operating of the Aluheat system. Data presented in this chapter is based on Publication IV.

3.1 Effective thermal conductivity

As mentioned in previous chapter, MgB_2 is a very promising candidate for many applications at temperatures ranging from 4.2 K to 30 K. However, there are still some stability issues with MgB_2 tapes [70]. One of the most important parameters that effects on the quench propagation and stability is the effective thermal conductivity that takes into account the whole composite structure of the coil. Thus, in conduction cooled coils, the knowledge of transverse effective thermal conductivity λ_{eff} is absolutely necessary for simulation of quench and for determining the safe operation conditions [74]. In general, λ_{eff} is a function of interfacial thermal contact resistances, thermal conductivities, geometric

distribution, volumetric fractions, and the dimensions of different components [22]. We measured the λ_{eff} of the MgB_2 coil cross-section and compared it with simulations. Bi-2223 was not studied since it is too expensive.

3.1.1 Sample preparation

Measurements were made for a small cut off section of the react-and-wind coil originally manufactured for demonstration purposes in order to test the suitability of MgB_2 for coils [72]. Coil was wound out of continuous piece of MgB_2 tape. The total conductor length was 46 m and the coil had 144 turns in total, i.e. six turns in every 24 layers. The fill factor of the coil was about 60.5% for the whole conductor and 5.6% for the superconducting MgB_2 part. Fig. 3.1 shows the dimensions of the sample coil segment. The MgB_2 tape was uninsulated, and therefore, a thin sheet of silk paper was interleaved between the layers. Resin impregnation with epoxy was carried out using the wet layer technique. Layers were insulated from each other by co-winding a mono filament nylon fishing line with a diameter of 0.5 mm adjacent to the tape. The cross-section of the measured coil segment is presented in Fig. 3.2. Since the coil is small, even small changes in dimensions have a huge effect

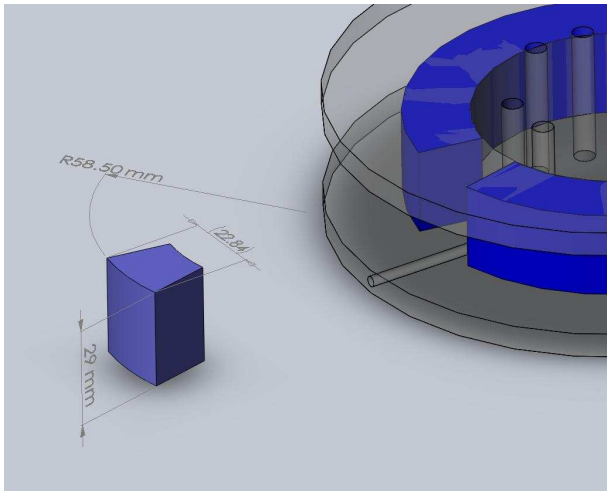

Figure 3.1: Dimensions of coil segment used in measurements.

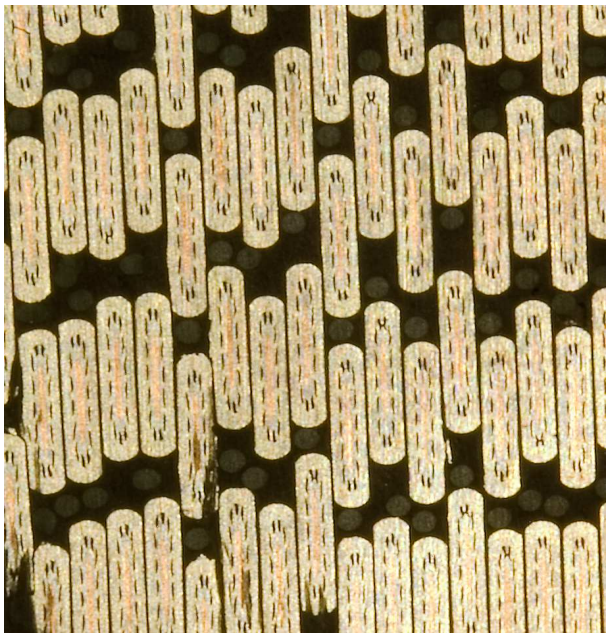

Figure 3.2: Enlarged picture of cross-section of measured coil. Layers were insulated by co-winding nylon fishing line adjacent to tape that can be seen as black dots in the figure.

on the fill factor, and thus, the fill factor of the coil varied between 57% and 64%. However, the average fill factor of 60.5% was used in the simulations. A two-stage G-M cryocooler was used for cooling.

3.2 Simulation

In order to make a good coil, simulations are used to optimize the design parameters. Next, we construct a simulation model to see if it correlates with measured results. Fourier's law links together the heat flux density (q) and the temperature gradient

$$q = -\lambda(T)\nabla T, \tag{3.1}$$

where λ is the thermal conductivity and T is the temperature. Inside a macroscopic body, the λ_{eff} can be determined as

$$\lambda_{\text{eff}} = \frac{l}{A\Delta T}\int_A q da, \tag{3.2}$$

where ΔT is the temperature difference between the ends, l the length and A the cross-sectional area of a body while the integration is performed over the cross-section. When thermal conductivities and volume fractions of component materials are known, one can calculate the upper and lower limits for the λ_{eff} by utilizing the analogy with electrical circuits [43]. Therefore, the lower and upper limits correspond to the thermal conductivity in perpendicular and in parallel to the layers of the composite. The upper limit in superconducting coils equal the λ_{eff} along the tape when the superconducting filaments are non-twisted. The upper and the lower limits of λ_{eff} are explained in detail in [46]. For determining the transverse λ_{eff} of the coil, a numerical model was used. Here, λ_{eff} was computed from the unit cell assuming ideal thermal contacts between the constituents [46]. In the model, the boundary conditions were derived from symmetry. Constant temperature boundaries were set on both ends of the unit cell, and no heat was flowing through the sides. The boundary conditions and unit cell configuration are shown in the Fig. 3.3. Used material data was obtained from [48, 55, 64]. In the simulations, the effect of the nylon fishing line was excluded.

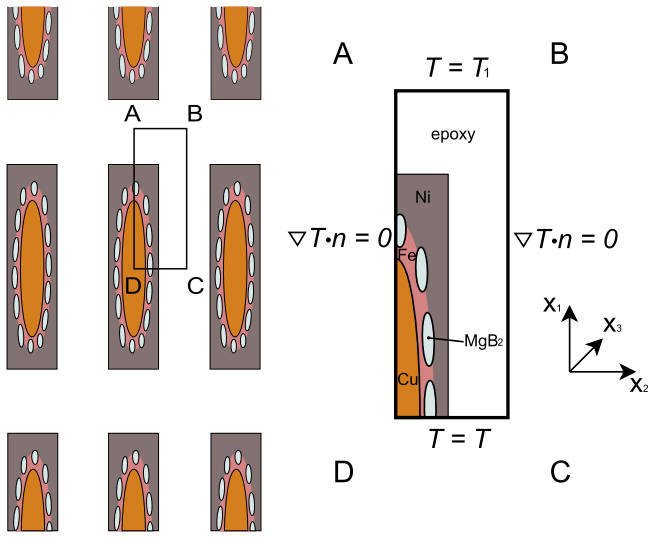

Figure 3.3: View of coil cross-section and unit cell structure. Boundary conditions to determine effective thermal conductivity in X_1-direction in the cross-section of the HTS coil are also presented. The figure is out of scale.

3.3 Measurements

Directions parallel to the broad tape face, perpendicular to the broad tape face and along the tape were denoted as X_1, X_2 and X_3, respectively. These directions are also shown in Fig. 3.3. In measurements along X_1-direction, the heater and the Cernox 1050 temperature sensor were fixed to the small copper plate attached to the bottom of the sample while the cooling interface along with another Cernox was located at the top as shown in Fig. 3.4. All the measurement leads were thermally anchored to the copper to eliminate the heat conduction via the leads. In perpendicular thermal conductivity measurements, the cold head and the heaters were kept in their original place but the sample was turned 90 degrees. The radiation shield around the measurement system was at 66 K while the whole system was in a vacuum. In the heat flux measurements, the sample was insulated with ten layers of super insulation

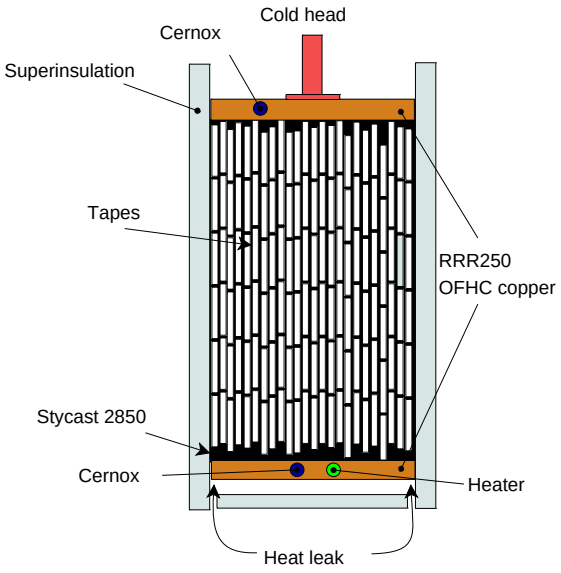

Figure 3.4: Cross section of the sample. Locations of the heater and temperature sensors at thermal conductivity measurements parallel to the broad side of the tape. Due to the seam at super insulation a small heat leak warmed the sample during the measurement. The radiation shield around the measurement system was at 66 K.

to keep the situation as thermally adiabatic as possible. The temperature of the upper sample surface was then varied between 10 and 35 K by a heater. Small heat through the seams at the bottom of the super insulation made the situation slightly non-adiabatic. The seams are also shown in the Fig. 3.4. When the heater was switched off, the temperature difference over the sample was 0.4 K and 0.9 K when measuring in X_1 and X_2-directions, respectively. Error caused by this heat leak can be eliminated from the results when the total heat leak through the sample is calculated as in Publication II.

3.4 Results

Fig. 3.5 shows the theoretical upper and lower limits for the λ_{eff} values and compares the measured and simulated λ_{eff} values as a function of temperature. As can be seen, simulated λ_{eff} in X_2 direction agreed well with the measured one. In the X_1-direction, the greatest difference was at 25 K temperature when the measured λ_{eff} exceeded the simulated one by 39 %. Differences between the measured and simulated results probably arose from the inaccurate material data of the epoxy and from the inhomogeneous fill factor of the hand wound coil. In both cases, the simulated and measured thermal conductivities crossed each other roughly at 15 K temperature. This might suggest that the contact resistances could be negligible in the measured sample since, despite ignoring them in the simulation, higher λ_{eff} was obtained in the measurements. Along the tape (X_3-direction), the λ_{eff} was over two orders of magnitude higher compared to the other directions. The theoretical lower limit of λ_{eff} at 20 K was 0.13 W/mK, while the measured λ_{eff} was 0.3 W/mK at its lowest at the same temperature. Thus, some stability estimates for an MgB_2 coil could be made using easily calculable lower limit data.

Fig. 3.6 shows how the fill factor affects λ_{eff}. If the fill factor increased, λ_{eff}-values rose greatly. With fill factors below about 80%, the effective thermal conductivity is dominated by the epoxy content in the coil. To explain the difference between the simulated and measured results, the fill factor of the

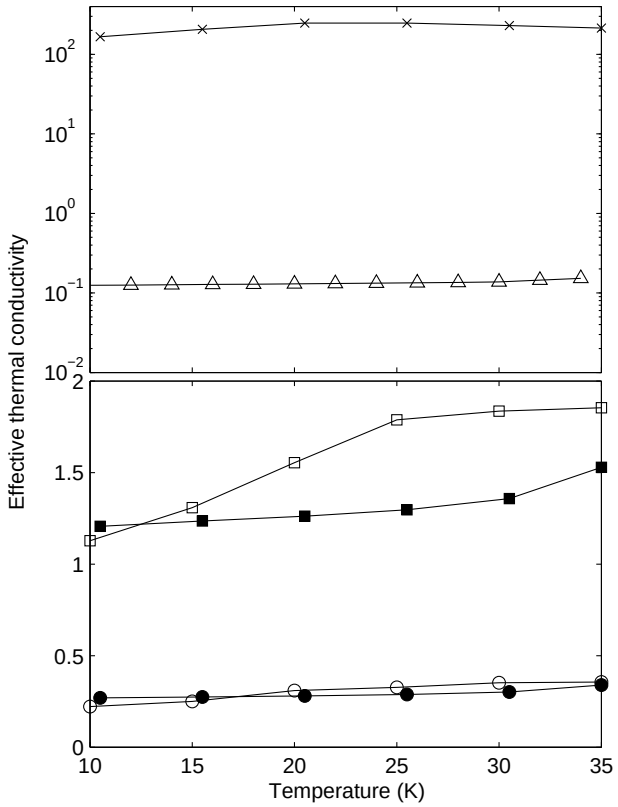

Figure 3.5: Upper figure shows upper(×) and lower limits(△) of effective thermal conductivities. Lower figure shows simulated effective thermal conductivities in (■) X_1 and (•) X_2 directions between 10 and 35 K. Measured effective thermal conductivities in X_1(□) and X_2(○)-direction are also presented.

coil would have had to be around 75%. However, as mentioned before, the fill factor of the coils was estimated to vary between 57% and 64% only. Within these limits at 20 K, the simulated thermal conductivity ranged between 1.1 and 1.5 W/mK in the X_1-direction and between 0.25 and 0.29 W/mK in the X_2-direction. Other errors arise because in the simulation all the filaments were assumed to be elliptical, the unit cell used in the simulation represents perfectly periodic coil, and the material properties used in the simulation are not accurate. The non-periodic structure of the coil increases the thermal conductivity in the X_1-direction when heat is allowed to zigzag through the

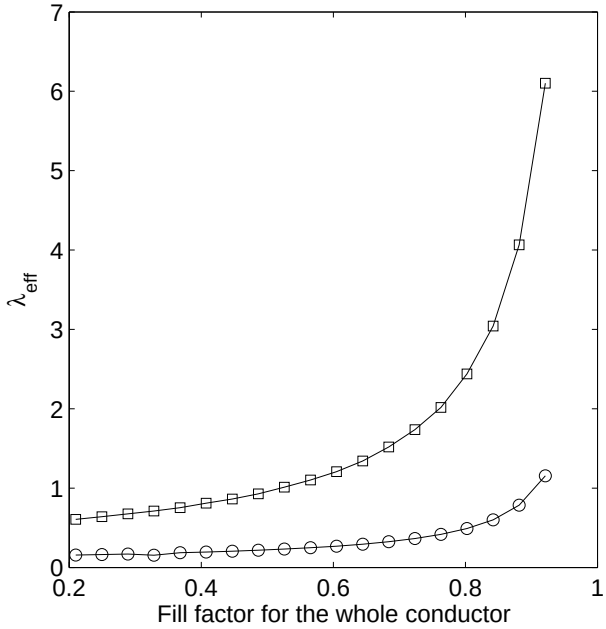

Figure 3.6: Simulated effective thermal conductivity in the X_1-direction ($\square$) and in the X_2-direction ($\circ$) at 20 K as a function of the fill factor of whole conductor.

coil with little epoxy on its way as shown in Fig. 3.2. When studying the sensitivity results against the thermal conductivity of the used materials, it was found that the epoxy is the key element for improving λ_{eff} in MgB_2 coils. Varying thermal conductivity of other materials had little or virtually no effect on the λ_{eff} of the coil with a fill factor of 60.5%. Fig. 3.7 shows the difference of λ_{eff} ($\Delta\lambda_{\text{eff}}$) in X_1- and X_2-directions at 20 K when the thermal conductivity of epoxy have been multiplied with the factor of k. When the fill factor climbed roughly over 80% the sensitivity still depended almost linearly on the change in k, but the coefficient of proportionality was 4.5 times larger in the X_1-direction than in the X_2-direction. However, the thermal conductivity of other materials became significant as well. Simulations showed that iron and copper mostly affected the λ_{eff} in the X_1-direction, while nickel and iron contributed the most in the X_2-direction.

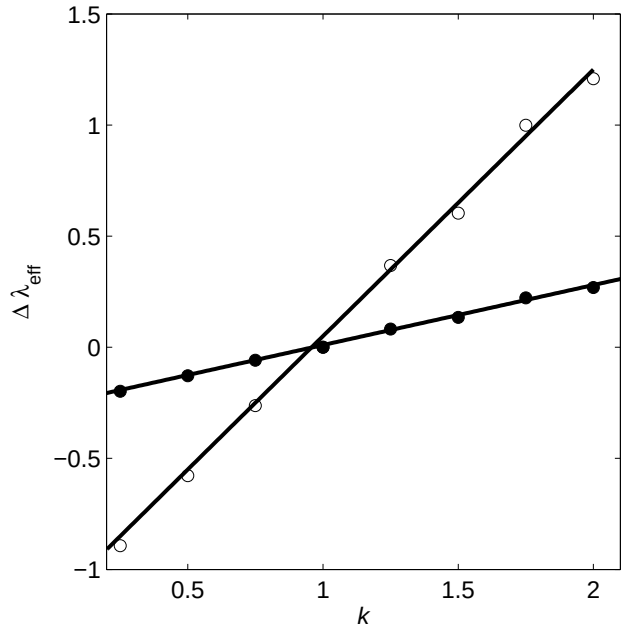

Figure 3.7: Sensitivity of effective thermal conductivity of epoxy with X_1 (○) and X_2 (●)-directions when the thermal conductivity of the epoxy has been multiplied with the factor of k at 20 K. Fill factor of the coil was 60.5% for the whole conductor.

3.5 Conclusions

The effective transverse thermal conductivities in a MgB_2 coil were measured and simulated. The measured thermal conductivity in the coil at 20 K in X_1- and X_2-direction was about 1.55 W/mK and 0.31 W/mK, respectively. Although the measured data gave higher λ_{eff} values than simulated ones at temperatures exceeding 15 K, the simulated and measured data agreed fairly well. Differences arose from the inaccurate material data, imprecise coil fill factor and non-periodic coil structure. In general, the simulated λ_{eff} in the X_1-direction was about four times higher than in the X_2-direction, while λ_{eff} in the X_3-direction was over two orders of magnitude higher compared to the other directions. Sensitivity calculations were also performed to evaluate which material affects most λ_{eff}. Results show that the thermal conductivity of epoxy

is by far the most important property when λ_{eff} is considered. When fill factor of the coil climbed about 80% iron and copper started to affect most to λ_{eff} to X_1-direction while nickel and iron contributed most to X_2-direction.

Chapter 4

Current leads

Last chapter presented the effective thermal conductivity which is one of the key parameters needed in stability and quench calculations. Next, I introduce important parameters, needed while designing HTS current leads. These parameters comprise contact resistance, thermal resistance and thermal conductivity. First, large contact resistance at the current leads might generate excessive heat load to the cryocooler and in the worst case can cause overheating of the leads. Second, elevated thermal resistance affects the temperature profile of the lead and may results in a premature quench. Last, thermal conductivity through the lead has to be minimized because it adds heat load to the lower end of the current lead and decrease system performance. In this chapter, I evaluate these design parameters in the HTS lead by varying used solders at both ends of the lead. The presented data is based on Publication II.

4.1 Contact resistances in current leads

In conduction cooled superconducting coils, HTS current leads are often used. Conventional copper or brass leads can be used to transport the current from room temperature to the temperature of the radiation shield, but HTS leads are recommended for the lower part down to the coil [26]. This is due to the fact that HTS leads generate no Ohmic losses in the lead itself and the

thermal conductivity of the lead is relatively small. Therefore, the heat load via HTS current leads is significantly lower if compared to the best possible conventional leads, and thereby, operating costs are reduced [12, 25, 29, 30]. HTS current leads are usually made with HTS tapes or with a HTS bulk in between high conductivity copper terminals. When the HTS bulk is used, the heat load can be four times smaller compared to the HTS tapes [23]. However, then there can be problems with electrical and mechanical stability [60]. Thus, HTS tapes with a high conductivity matrix offer a good compromise between stability and thermal conduction. Fig. 4.1 shows an example of current input from Aluheat project.

There are many different ways to attach the HTS lead to the copper terminals but soldering seems to be most commonly used. The choice of soldering material aims to have good electrical and thermal contact in the joints to minimize the losses and to ensure efficient cooling of the lead. Contact resistances and heat flux through the lead are the two major components that contribute

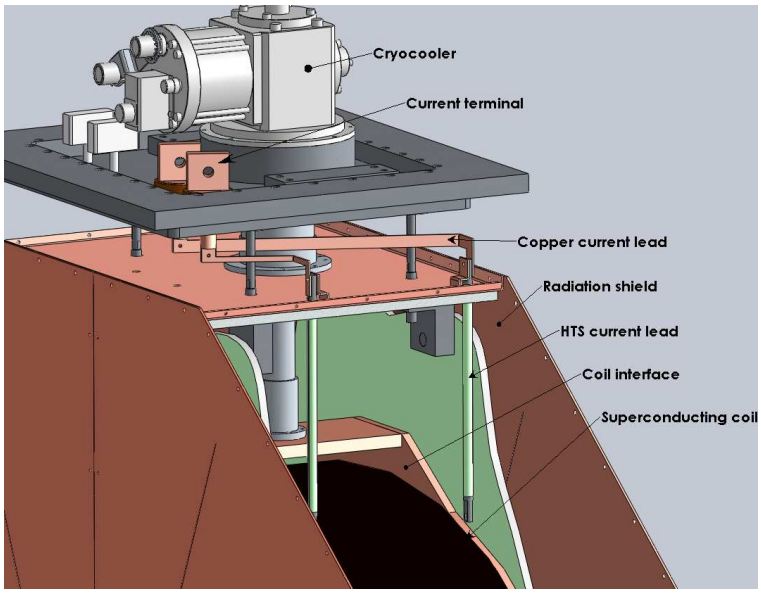

Figure 4.1: Current input in Aluheat project. Conventional copper leads transport the current from room temperature to the temperature of the radiation shield. HTS leads are used for the lower part down to the coil.

to the total heat load to the coil. Moreover, the current leads can comprise a significant part of the system's total losses. Therefore, many papers study the contact resistances between HTS and copper in current lead applications [6], but they seldom report in detail how the joints were actually made [80]. Furthermore, there are only a few studies about the thermal conductance over the soldered joints in cold temperatures even though it is an important design parameter in current leads since it determines the temperature profile of the superconductor. A large thermal contact resistance may result in poor cooling and degrade the current carrying capacity [80]. Moreover, complete design and simulation of current leads and joints is difficult since even if there is a lot of published data of material properties in cryogenic temperatures they are often hard to find [10, 55].

Next I study various soldering materials and the electrical and thermal resistances over the soldered joints measured in a vacuum at different temperatures for current leads manufactured of BSCCO tape. Furthermore, I measure the heat leak through the constructed current lead and compare the performance with commercial leads. Finally, a proposal to make efficient current leads for the current range of 0-1000 A is shown.

4.1.1 Preparation of the current leads

Current leads were manufactured using G-10 epoxy rod with RRR 100 copper terminals at both ends as shown in Fig. 4.2. The total length of the lead was 300 mm and diameter 14 mm. BSCCO tape was then installed to the 275 mm long groove in the rod. When the one end of the lead was cooled down to 20 K the other end was at 77 K lead I_c was 250 A. The tape had thin steel supports on both sides but they were mechanically removed from the current terminal area when the tape was soldered to the copper terminals over the 32 mm distance. The tape width of 4.1 mm made the total contact area of each joint to about 1.31 cm^2.

Before soldering both contacts were cleaned with acetone, fine sandpaper

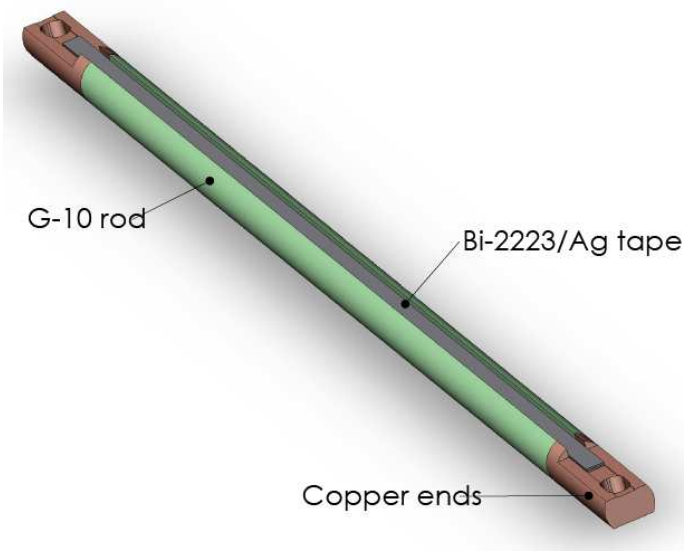

Figure 4.2: Scheme of current lead.

and soldering liquid containing 14% of zinc chloride and 7% of ammoniumchloride. AIM manufactured RMA 201 paste flux was also used with the solders since it has good wetting properties and large process window. Contact and thermal resistances were measured with voltage taps and Cernox 1050 temperature sensors on both sides of the soldered contacts as shown in Fig. 4.3. In addition to the solder material the contact resistances depend on the quality of the work. To verify the reproducibility of the contacts five similar samples were made with conventional 50Sn/50Pb solder. Then, the contact resistance varied between 2124 and 2188 nΩcm^2 at 77 K. Thus, the variation was about $\pm$1.5%. Next, five separate current leads were made with different solders that included 52In/48Sn, 97In/3Ag, 90In/10Ag, 96.5Sn/3.5Ag and 99.3Sn/0.7Cu solders. Pure indium solder was not studied although it is commonly used in cryogenic applications since there are already many studies about the properties of indium [68, 75]. Used solder properties are presented in Table 4.1, where σ_{u} is the tensile strength of the material, γ the electrical conductivity in per cent of International Annealed Copper Standard (IACS%) and $\lambda_{85\mathrm{c}}$ thermal conductivity at 85 °C. Indium is also presented in the table for comparison. Pure indium and In52/Sn48 exhibit the best wetting quality on non-metallic.

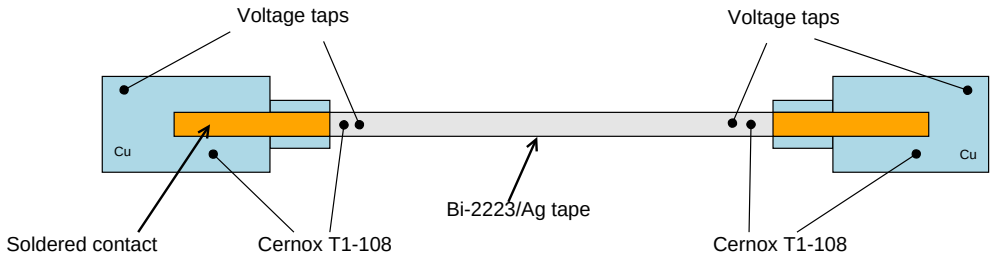

Figure 4.3: Voltage tap and temperature sensor locations over the soldered joint.

90In/10Ag and 97In/3Ag exhibit slightly lower wet ability but higher strength due to the hardening effect of the silver [3]. More solder properties at low temperatures of Sn/In and Sn/Ag solders can also be found in [35].

4.1.2 Contact resistances and Ohmic losses

Contact resistances were measured between 20 K and 77 K with cryocooler and heater. A current of 10 - 50 A was fed through the current lead and the voltage was measured over the joints with voltage taps soldered to the lead. Results are shown in Fig. 4.4. The difference between contact resistances at 77 K was 72% as 96.5Sn/3.5Ag solder had the highest contact resistance of 996 nΩcm^2 and 90In/10Ag had the lowest value of 275 nΩcm^2. At 20 K the 90In/10Ag had lowest contact resistance of 45 nΩcm^2 and 96.5Sn/3.5Ag had the highest contact resistance of 121 nΩcm^2. The differences between the con-

Table 4.1: Properties of studied solders around room temperature.

Composition	Liquidus (°C)	σ_u (MPa)	γ IACS%	λ_{85c} (W/cmK)
100In	157	1.88	24	0.86
52In/48Sn	118	11.86	11.7	0.34
90In/10Ag	237	11.38	22.1	0.67
97In/3Ag	143	5.52	23	0.73
99.3Sn/0.7Cu	227	29.65	13	N/A
96.5Sn/3.5Ag	226	26.70	14	N/A

[3, 5, 10]

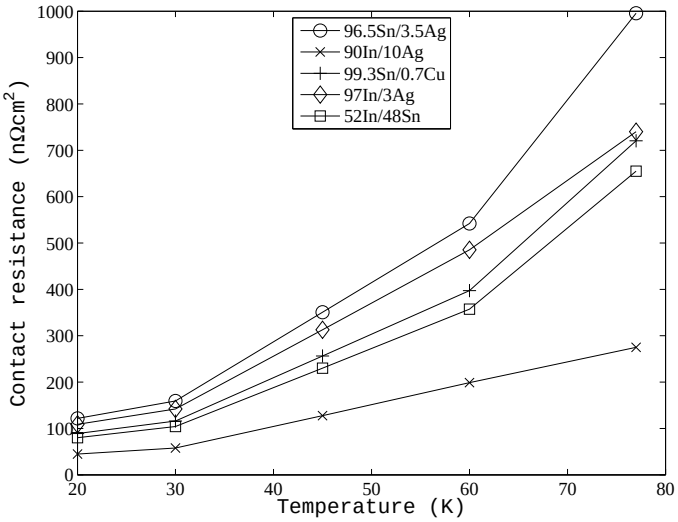

Figure 4.4: Measured contact resistances at different temperatures.

tact resistances at 77 K can be significant concerning the temperature profile and lead to degraded performance at high currents. In vacuum conditions the contact resistances can be increased compared to the normal pressure because possible small cracks and voids can become totally insulating. The influence of the vacuum pressure was checked at 10^{-8} - 10^{-4} mbar but no variation was found in the results. Thus, all the measurements were carried out at a vacuum pressure of around 10^{-7} mbar.

4.2 Thermal resistances and heat leak

In the thermal heat flux measurements, the current lead was insulated with six layers of super insulation which corresponds to a typical structure in magnet systems. The lower end of the leads was then cooled down to 20 K with a cryocooler while the upper end was connected to a heater. In addition to the power of the heater, P_h, also the radiated heat load, P_a, through the super insulation was warming up the lead. Then, the heat flux density in the current lead can roughly be estimated as

$$q = (P_\mathrm{h} + P_\mathrm{a})/A, \tag{4.1}$$

where A is the cross-section of the current lead. On the other hand, when the heat transfer through complex structures is investigated the total heat transfer coefficient, (U), is commonly defined so that

$$q = U(T_{\mathrm{w}} - T_{\mathrm{c}}), \tag{4.2}$$

where T_{w} is the temperature at the upper end of the lead and T_{c} temperature at the lower end of the lead. Combined equations 4.1 and 4.2 result in

$$P_{\mathrm{h}} = UAT_{\mathrm{w}} - UAT_{\mathrm{c}} - P_{\mathrm{a}}. \tag{4.3}$$

That is, P_{h} should be a first degree polynomial of T_{w} as

$$P_{\mathrm{h}} = xT_{\mathrm{w}} + y \tag{4.4}$$

where x and y are unknown constants. For example, x and y can be determined with the least squares fitting when the measurements are repeated at different values of T_{w}. Finally

$$P_{\mathrm{a}} = -(y + xT_{\mathrm{c}}). \tag{4.5}$$

and the total heat leak in the lead can be estimated as $P_{\mathrm{t}} = P_{\mathrm{a}} + P_{\mathrm{h}}$.

It is worth noting that in practice P_{a} depends on T_{c}. Furthermore q is not constant in the lead but due to the radiated heat load it increases towards the lower end. Thus, P_{a} determined here represents an effective radiated power. The total heat transfer coefficient $U = x/A$ can be used to compare the overall performance of different current lead structures [66]. Here the temperature of the upper end leveled at 30 K when the heater was off. Next the upper end temperature was lifted progressively and the needed heating power at the upper temperatures of 45, 60 and 77 K was measured. Table 4.2 shows the measured temperatures and corresponding heat leaks through the sample.

4.2.1 Thermal contact conductances

To determine the thermal resistances of the joints the temperature difference over the joints was measured at different temperatures. In the measurements

Table 4.2: Measured heat leaks through the current lead at T_c=20 K.

T_w	30 K	45 K	60 K	77 K
P_t	16 mW	37.5 mW	59 mW	83.6 mW

the temperature at the lower end of the current lead was again kept at 20 K and the temperature of the upper end was varied with a heater. Cernox 1050 temperature sensors were attached over both joints and the temperature differences measured. Location of sensors is presented in Fig. 4.3. Heat transfer coefficients (U_b) were calculated using the classical steady state method

$$q = U_b(T)(T_1 - T_0), \tag{4.6}$$

where $T = (T_1 + T_0)/2$ in the mean temperature of the joint. Fig. 4.5 shows the variation of thermal conductances with different solders at temperatures between 25 K and 77 K. With all solders the thermal conductance decreased from 25 K to 60 K but after that it started to increase slightly again. A thermal conductance minimum has been suggested also in Ref. [80] in which Woods metal was used as a solder.

4.3 Design of the current leads

Based on the results of thermal and electrical resistances, HTS leads for conduction cooled applications were designed. Here 99.3Sn/0.7Cu was chosen as a solder. It had a contact resistance of 89 $n\Omega cm^2$ at 20 K and 720 $n\Omega cm^2$ at 77 K. Although the contact resistance was not the lowest possible, it had a good thermal conductance at 77 K. This is important since poor thermal performance at both ends can lead to unsatisfactory cooling. Also the solders mechanical strength is good according to the room temperature values. Using 99.3Sn/0.7Cu solder the Ohmic losses at 250 A were 4.3 mW and 34 mW at 20 K and 77 K, respectively. The thermal conductances over the joint in 25 K and in 77 K were 167 W/m^2K and 107 W/m^2K, respectively. Losses are generated at both ends of the lead but since the cooling power is a lot smaller

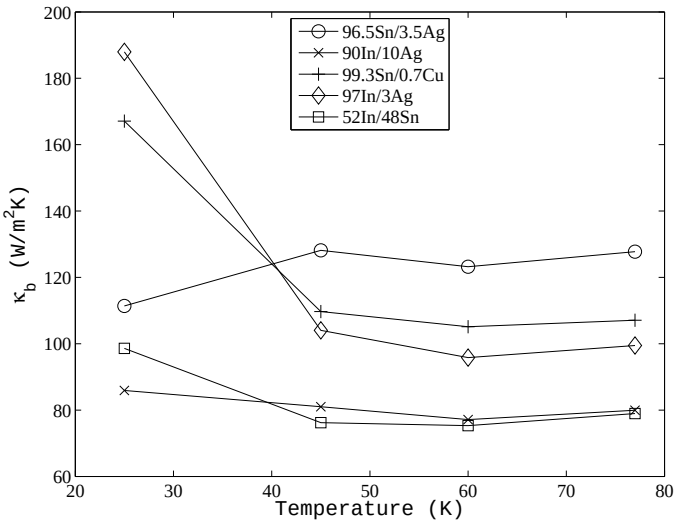

Figure 4.5: Thermal conductances over the joints at measured temperatures.

at the cold end of the lead the cold end losses become more significant. The total heat load of the designed current lead was compared with the commercial 250 A lead properties of which are presented in Table 4.3, where P_o is Ohmic heat losses at the cold end of the lead. Ohmic losses are omitted from the Table 4.3 since current lead manufacturers usually present only the heat flux through the lead. Also the Ohmic losses are usually less than 10% of the total losses, and thus, quite insignificant compared to the heat leakage. The heat flux through the lead is obtained from Table 4.2.

High current capacity leads can be made when several HTS tapes are connected in parallel. Fig. 4.6 shows the total losses in the current leads

Table 4.3: Comparison between commercial HTS Cryosaver leads and designed current leads with 250 A.

Loss component	**Commercial lead between 4.2-64 K**	**Designed lead between 20-77 K**
P_t	45 mW	83.6 mW
P_o	N/A	4.3 mW

In commercial leads, Ohmic losses are not usually revealed. [9]

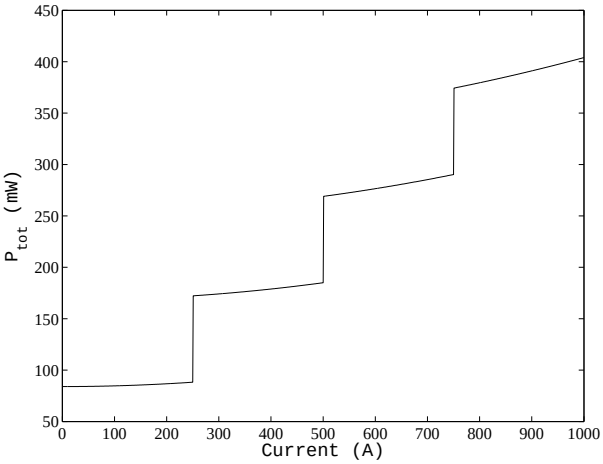

Figure 4.6: Total losses of current lead containing one to four leads in parallel when temperatures at cold and warm ends are 20 K and 77 K, respectively.

soldered using 99.3Sn/0.7Cu with the function of amperage when one to four leads are soldered in parallel and the lead operates between 20 K and 77 K, respectively. The losses at 1 kA level were 404 mW which is twice as high as had been measured in Ref. [23]. However, contact resistances were about the same. That is, the high losses were generated due to the heat leakage because the used tape was not optimized for current lead applications [76].

4.4 Conclusions

The thermal conductance and electrical resistances of the different solder materials as well as their applicability to the HTS current leads were studied. Five similar current leads were constructed except that different solders were used in the contacts between the BSCCO tape and the copper terminals. The solders included 52In/48Sn, 97In/3Ag, 90In/10Ag, 96.5Sn/3.5Ag and 99.3Sn/0.7Cu. Results show that the indium based solders were viable choices for current leads due to their wet-ability and properties at low temperatures. However, I selected the 99.3Sn/0.7Cu solder for our current leads since it has a good combination of electrical, thermal and mechanical properties.

Chapter 5

Sample characterization, losses and stability

Accurate data about the voltage current behavior at different temperatures is imperative for the designers of various superconducting applications. Next, I present a method, originally presented in publication V, to solve the intrinsic critical current and n-value using apparent $V(I)$-data and verify the method in experimental study, originally presented in publication VI. For the method to work accurately, the sample or coil should be measured in adiabatic conditions. Completely adiabatic conditions are impossible to achieve but can be approximated by cooling the sample using a cryocooler and a specially designed low conductivity sample holder in a vacuum atmosphere. In general, adiabatic measurements are difficult since the sample might burn up. However, this can be avoided if proper quench detection is in place [73].

5.1 Effects of temperature on voltage current curves

To measure short sample $V(I)$-curves reliably, cooling has to overcome the generated losses and keep the temperature stable. Liquid cooled systems introduce sufficient cooling in most cases, but in conduction cooled systems, the stable temperature may be easily lost. By using a slow current ramp rate,

the generated losses can be extracted and temperature kept constant up to the point when the voltage starts to increase rapidly. When fast current ramp rates are used, other problems arise due to the inductive coupling and AC-losses. Superconducting short samples are usually characterized by measuring the voltage $V(I)$-curve at a desired temperature as explained previously in the second chapter. To get reliable results, the temperature should remain constant within a few 10 mK margin during the $V(I)$-curve recording. [49]. However, when the current is ramped up, heat is generated due to the resistance of sample contacts as well as due to the ohmic losses even at sub critical currents. Fig. 5.1 shows in principle how the ramp rate affects to the $V(I)$-curve.

In a conduction cooled measurement station, the sample is usually attached to a sample holder with high thermal conductivity. The sample holder tries to ensure uniform temperature over the sample and helps to extract the losses. Losses generated in sample contacts are usually small enough to be extracted by the cooling system. However, as the critical current is approached, the voltage starts to increase rapidly inside the sample, and heat has no time to conduct away. Thus, the sample warms up distorting the most important part of the $V(I)$-curve. This effect degrades I_c and increases n-value.

Due to a modest thermal conductivity in superconductors and slow response of the temperature sensors, these changes can be difficult to detect,

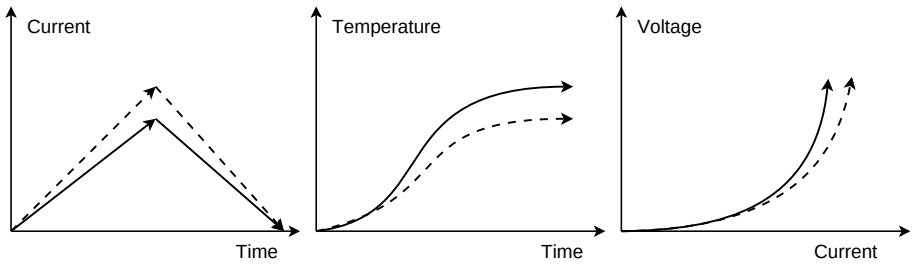

Figure 5.1: Warming of the sample distorts the $V(I)$-curve at subcritical currents. Solid line and dashed line represents slower and faster current ramp rate measurement, respectively.

and they may remain unnoticed, especially while measuring superconducting coils. For example, the typical response time of a Lakeshore manufactured copper canister packed CX-1050 (AA) temperature sensor is 2 s at 77 K and around 1 s at 25 K [8]. Thus, the temperature just before the quench is difficult to measure. Increasing the current ramp rate reduces the ohmic losses but generates other loss components like AC-losses. Furthermore, high current ramps can make the measurement inexact due to the voltage induced to the measurement wires or due to the insufficient sampling frequency [63].

Using lower E_c will also improve the results since less ohmic losses are generated before I_c is attained. However, lowering E_c easily leads to a very bad signal to noise ratio in the measured data and many laboratories are not able to measure I_c of a short sample below E_c of 0.1 μV/cm. Also, in some applications, like in fault current limiters, $V(I)$-curve data at high currents and voltages are needed as well. Furthermore, false n-values may lead to bad coil designs [28, 49].

5.2 Method to improve voltage current curves

The main idea is to measure $V(I)$-curves during both the ascending and descending branches of a triangular current ramp. If a lower critical current is measured during the descending ramp than during the ascending ramp, it reveals that there are problems with sample heating. Furthermore, these problems can be removed because the actual constant temperature $V(I)$-curve can be calculated without knowing the real temperature increase in the sample during the measurement. The temperature dependence of I_c is here considered linear, and therefore, expressed as

$$I_c(T) = xT + y, \tag{5.1}$$

where x and y are unknown constants and T the sample temperature. When current flows through the sample, the temperature increases due to the ohmic losses generated near I_c, and thus, the critical current changes. When the

current reaches I_{c1} in the ascending ramp, the sample temperature T_1 is given by

$$T_1 = T_0 + \frac{Q_1}{C_p}, \tag{5.2}$$

where T_0 is the initial sample temperature, Q_1 the heating energy during the ramp from zero current to I_{c1} and C_p the specific heat. Here, I assume that C_p is independent of temperature. Similarly, the sample temperature T_2 at I_{c2} in the descending ramp can be expressed as

$$T_2 = T_1 + \frac{Q_2}{C_p}, \tag{5.3}$$

where Q_2 is the heating energy during the ramps between the I_{c1} and I_{c2}. Fig. 5.2 shows schematically the relation between different critical currents and the measured $V(I)$-curve.

Heating energy Q_1 can be integrated from

$$Q_1 = \int_0^{t_{c1}} VIdt, \tag{5.4}$$

where t_{c1} is the time when current I_{c1} is reached. Correspondingly,

$$Q_2 = \int_{t_{c1}}^{t_{c2}} VIdt, \tag{5.5}$$

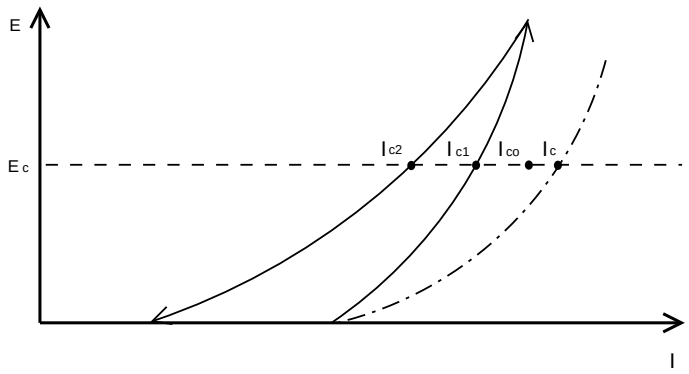

Figure 5.2: Schematical explanation about the relation between different critical currents and measured $V(I)$-curve. The solid line represents measured $V(I)$-curve, and the dash-dot line represents constant temperature $V(I)$-curve. I_{c1} and I_{c2} are critical currents in ascending and descending ramps, respectively. I_{c0} is corrected critical current and I_c constant temperature critical current.

where t_{c2} is the time when current I_{c2} is achieved. Q_1 and Q_2 are calculated in adiabatic conditions since the effect of the cooling is impossible to measure accurately in real measurements.

By combining Eq. (5.1) with Eqs. (5.2) and (5.3) we obtain

$$I_{c1} = x(T_0 + \frac{Q_1}{C_p}) + y \tag{5.6}$$

$$I_{c2} = x(T_1 + \frac{Q_2}{C_p}) + y \tag{5.7}$$

Then, the difference between I_{c1} and I_{c2} becomes

$$I_{c2} - I_{c1} = \frac{x}{C_p} Q_2 \tag{5.8}$$

and the difference between I_{c1} and the corrected critical current I_{c0} is

$$I_{c1} - I_{c0} = \frac{x}{C_p} Q_1. \tag{5.9}$$

Now, by combining (5.8) and (5.9) we get

$$I_{c2} - I_{c1} = \frac{Q_2}{Q_1}(I_{c1} - I_{c0}). \tag{5.10}$$

Thus, we finally obtain

$$I_{c0} = \frac{Q_1}{Q_2}(I_{c1} - I_{c2}) + I_{c1}. \tag{5.11}$$

Ohmic losses Q_1 and Q_2 can be calculated from the $V(I)$-curve, and the corrected I_{c0} can be found. In reality, C_p increases with T, and therefore, I_{c0} values are slightly below I_c. Nevertheless, according to the simulation examples of this thesis, Eq. (5.11) can be used to obtain very good results even from poorly measured $V(I)$-curves.

When I_{c0} values are calculated using Eq. (5.11) with multiple E_c values, the whole $V(I)$-curve can be corrected, and the real n-value obtained.

5.2.1 Short sample simulations

In the simulations, the short sample data of a BSCCO tape was used (Fig. 5.3). The tape cross-section area (A) was 1.23 mm^2, and the electric field criterion of 1 μV/cm was used. Simulated current ramp rates included 10, 5 and 2 A/s. Each ramp rate was studied at different temperatures between 20 K and 70 K. C_p used in the simulations was calculated as

$$C_\mathrm{p}(T) = (cT - d)A, \tag{5.12}$$

where $c = 1.5 \cdot 10^4$ J/m^{3}K^2 and $d = 2.2{\cdot}10^5$ J/m^{3}K [7, 20].

The ascending ramp started from 0 A. The current was allowed to increase until the voltage exceeded $1.4E_\mathrm{c}$. After that, the current was ramped to zero with a ramp rate of 10 A/s. AC-losses were neglected, and thus at high current

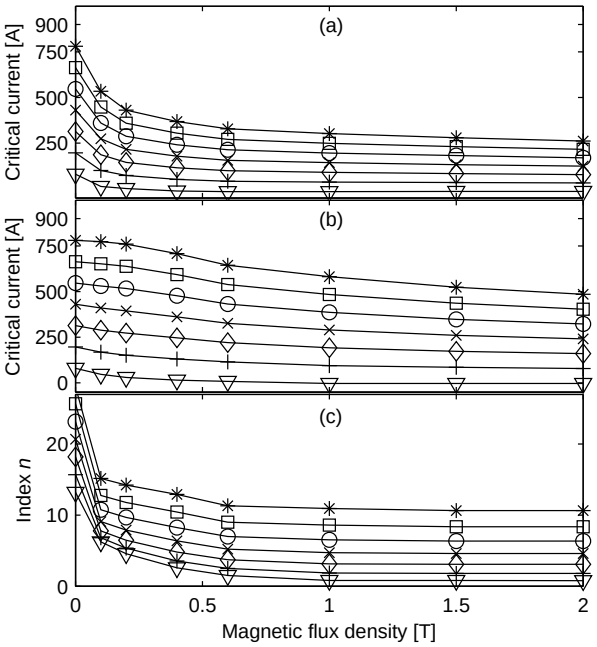

Figure 5.3: Measured short sample properties as function of external magnetic flux density for BSCCO tape: (a) critical current in perpendicular field, (b) critical current in parallel field, (c) n-value in parallel field. Curves correspond to temperatures of ($\star$) 20 K, ($\square$) 30 K, ($\circ$) 40 K, ($\times$) 50 K, ($\Diamond$) 60 K, ($+$) 70 K and ($\triangledown$) 80 K [47].

ramp rates, the simulated results approached the constant temperature curve.

Fig. 5.4 shows the simulated voltage - current -curves at 20 K. With 2 A/s current ramp, the sample warmed up the most, and thus, the $V(I)$-curve was strongly distorted. The 10 A/s $V(I)$-curve was closest to the constant T curve, but I_{c1} was still 14 A lower than I_c. Fig. 5.5 shows the corrected and constant temperature $V(I)$-curves at 20 K with different current ramp rates. At a ramp rate of 2 A/s, $I_{c1} = 742$ A was corrected to $I_{c0} = 770$ A, which was only 10 A below the constant T critical current. The influence of heating is much more visible in n-values. I used the least squares method to solve the n-values from the simulation data as well as from the corrected $V(I)$-curves. For example at a current ramp rate of 2 A/s, the uncorrected n-value was 88, but the corrected value of 35 was acceptably close to the constant T value of 28. The initial difference of the real and apparent n-values can lead to dramatic design errors when considering a maximum persistent mode operation current of a coil. Furthermore, resistivity is the most important parameter while designing fault current limiters. At 770 A, the error between the ideal and simulated resistivity was close to 100%.

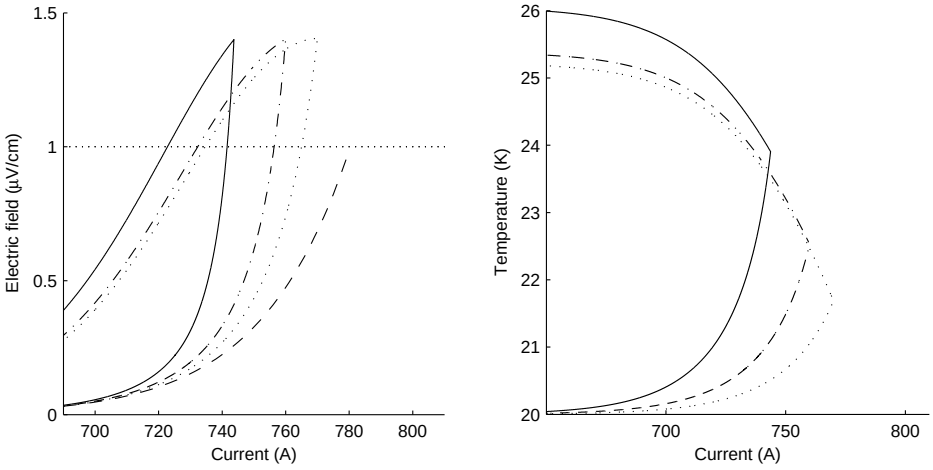

Figure 5.4: Simulated voltage - current curves and temperatures at 20 K. Corresponding to ramp rates of (solid line) 2 A/s, (dash-dot line) 5 A/s, (dotted line) 10 A/s. Dashed line corresponds to the constant temperature $V(I)$-curve. Considered electric field criterion is also shown.

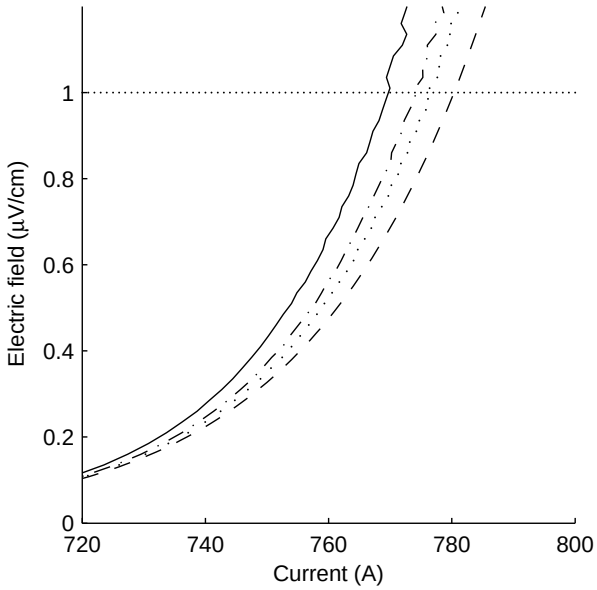

Figure 5.5: Corrected and constant T voltage current curves at 20 K. Curves corresponding to the ramp rates of (solid line) 2 A/s, (dash-dot line) 5 A/s, (dots) 10 A/s. Dashed line corresponds to the constant T curve. Electric field criterion of 1 μV/cm is also shown. Changing specific heat has taken into account, and thus corrected curves differ slightly from the constant temperature curve.

At 20 K, the specific heat of the sample and sample holder is small, and thereby, the error in uncorrected $V(I)$-measurements can be significant. Furthermore, I_c is high at low temperatures, and thus, ohmic losses are increased. When the temperature rises, the specific heat of the sample becomes higher and the critical current decreases so that the uncorrected simulated curves move closer to the constant T curves even at slow current ramp rates. Fig. 5.6 shows how the influence of heating decreases when the temperature rises from 20 K. Normalized I_c and n-values are calculated by dividing the simulated value with the actual measured value of the tape presented in Fig. 5.3.

At 2 A/s ramp rate, I_c was 2% higher than I_{c1} at 40 K, but using the correction method, the error was lowered to 0,1%. At 70 K and 2 A/s, the error between I_{c1} and I_c was only 0,58 A and, thus, needed no correction.

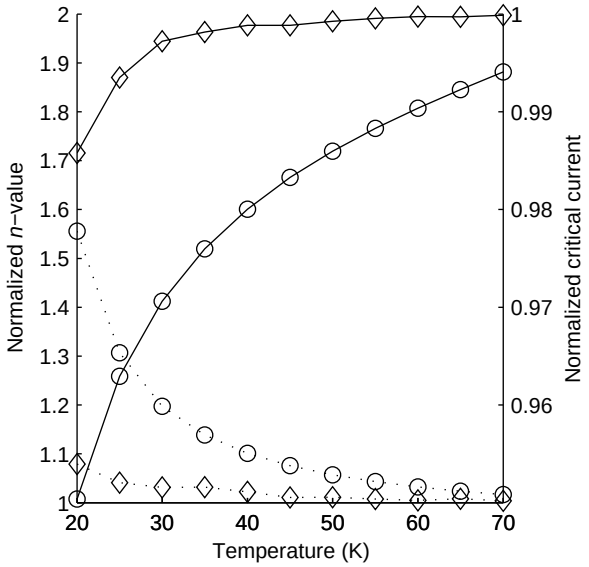

Figure 5.6: Normalized critical current (solid line) and n-values (dotted line): ($\Diamond$) corrected curves and ($\circ$) uncorrected curves. Current ramp rate of 2 A/s was used in simulations. Normalized I_c and n-values are calculated by dividing the simulated value with the actual measured value of the tape presented in Fig. 5.3.

To study the effects of warming on the different parts of the $V(I)$-curve, differential n-values, n_d, were also calculated as

$$n_d = \frac{dv}{di} = \frac{\partial v}{\partial i} + \frac{\partial v}{\partial T}\frac{\partial T}{\partial i} = n_0 + \frac{\partial v}{\partial T}\frac{\partial T}{\partial i}, \tag{5.13}$$

where $v = \log(V)$, $i = \log(I)$ and n_0 the real n-value at constant temperature. The term $\frac{\partial v}{\partial T}\ \frac{\partial T}{\partial i}$ is positive at the ascending ramp while changes into negative at the descending ramp. Differential n-values can be used here to interpret the simulations but they cannot be calculated from a real measurement due to the noise in the data. In real measurements n-value is evaluated fitting potential law between two chosen points near I_c using least squares method. Fig. 5.7 presents simulated differential n-values at 20 K, and it clearly shows that heating does not have any noticeable effect on the $V(I)$-curve until at 670 - 710 A depending on the ramp rate. After that, n_d increases rapidly, and when the 1 μV/cm criterion is reached, it exceeds 100 at 2 A/s and 50 even at 10 A/s. Thus, compensating the effects of heating becomes increasingly

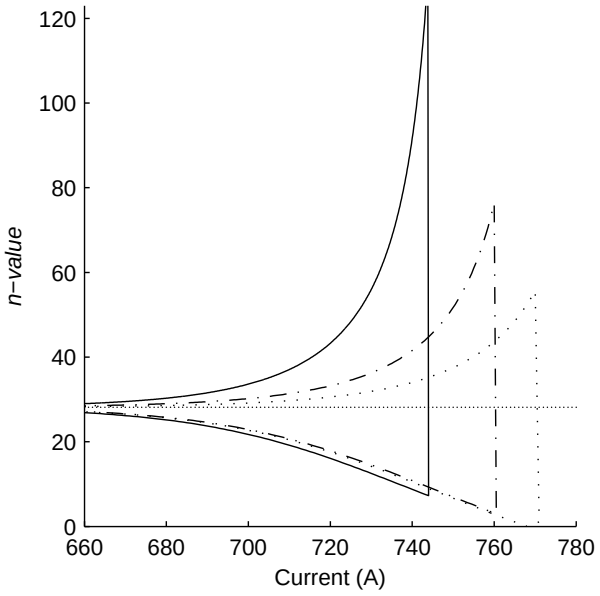

Figure 5.7: Differential n-values determined from simulated voltage current curves. Curves correspond to ramp rates of (solid line) 2 A/s, (dash-dot line) 5 A/s, (dotted line) 10 A/s. Actual n-value of sample (dotted line) of 28.

important if the data is used to design fault-current limiters where voltage current data is needed for the overcritical currents as well.

5.2.2 Short sample experimental setup

Both BSCCO tape and MgB_2 tape were studied. Different cooling methods were used for BSCCO tape and MgB_2 tape, but to make the correcting method work in both cases, the sample was made as thermally adiabatic as possible in both systems. When BSCCO tape was measured, the helium gas flow was cut before the measurement, thus, making the measurement as adiabatic as possible. In the conduction cooled case, i.e. when measuring MgB_2 tape, a specially designed adiabatic sample holder was used.

MgB_2 tape measurements

The MgB_2 tape was cooled with a cryocooler, that is, the measurements were carried out in a vacuum at 30 K. A specially designed low conductivity sample holder was used in these measurements. A 30 cm long sample was placed into a nylon groove and veiled with 20 layers of super insulation to make the situation as thermally adiabatic as possible. Both ends of the sample were fixed to the copper current terminals with 97Sn3Ag solder which is a good option at low temperatures as shown in the previous chapter. Voltage was measured using two voltage taps 98 mm apart using a HP nanovolt meter. To verify the measurement temperature before the measurement a Cernox 1050-AA was placed into a small copper cylinder located at the middle of the sample. Fig. 5.8 shows the picture of the sample holder. The current terminals were cooled to a fixed temperature with a combination of cryocooler and heater.

The measurement curves were corrected by using the correction method. Figs. 5.9 and 5.10 show the I_c and the n-value of MgB_2 tape of both, ascending and descending, current ramps as well as the corrected values with various current ramps at 30 K.

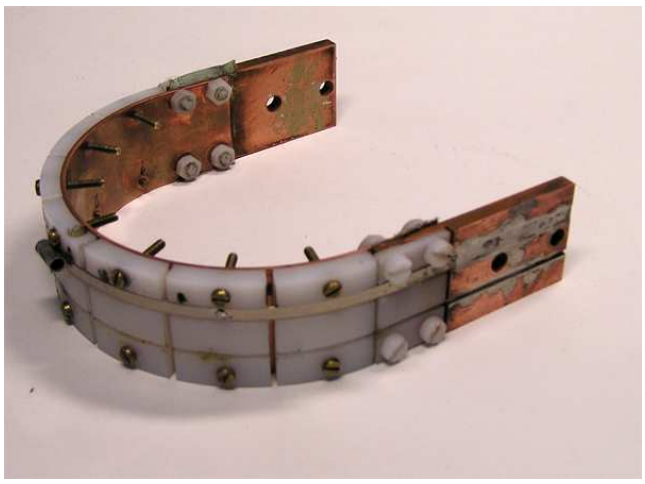

Figure 5.8: Picture of the sample holder. Only the uppermost of two sample grooves was in use. The place for temperature sensor can be seen in the middle of the sample.

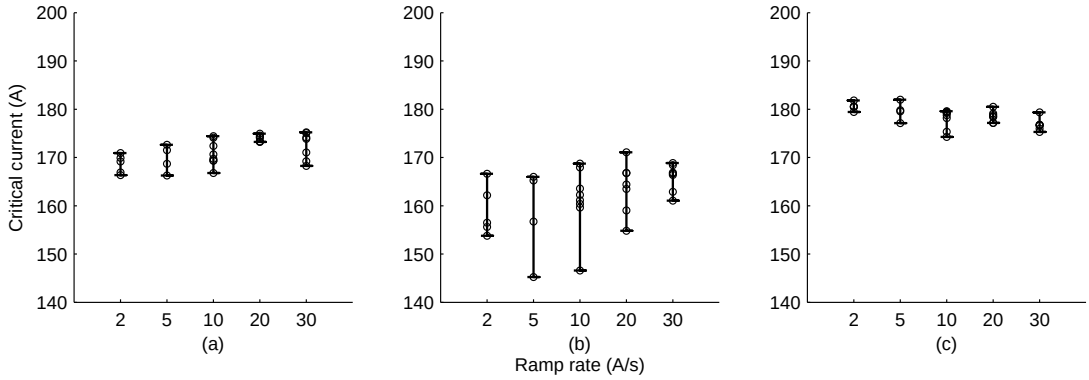

Figure 5.9: Measured I_c values of MgB_2 tape at ascending (a), descending (b) and corrected values (c). Initial temperature was 30 K. At each ramp rate, several measurements were made for consistency.

I_c values at the ascending ramp are the lowest at low current ramp rates when the sample warms up the most. The corrected I_c values are closest to the constant temperature values for the used MgB_2 tape at 30 K. The average of corrected I_c values varied between 177 A and 181 A.

In n-value measurements, shown in Fig. 5.10, the measured n-values from the ascending curve at the low current ramp rate were much higher than the actual n-values due to the heating in the sample. At high ramp rates, n-values

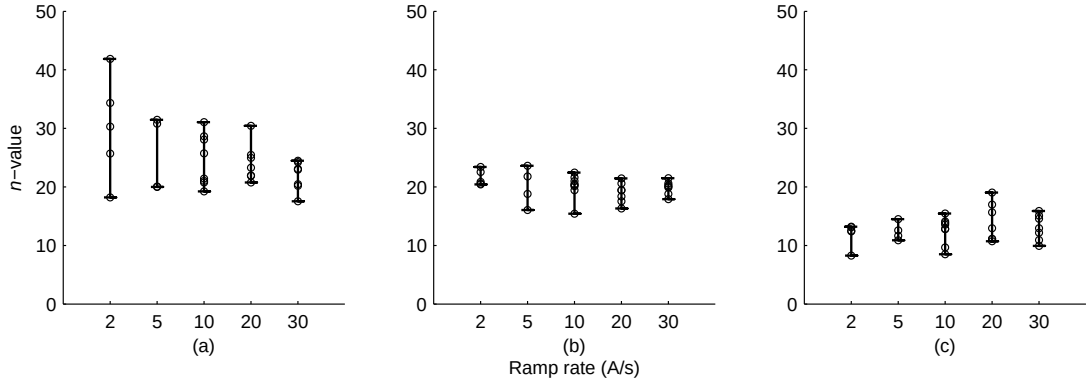

Figure 5.10: Measured n-values of MgB_2 tape at ascending (a), descending (b) and corrected values (c). Initial temperature was 30 K. At each ramp rate, several measurements were made for consistency.

decreased but were still far from the actual constant temperature n-value. n-values at descending ramps were more consistent with the ramp rate but still too high compared to the real n-value. Corrected values were closer to the real n-value, and the average of corrected n-values at different ramp rates varied from 11.9 to 13.4. However, at the 20 A/s ramp the difference between the highest and lowest n-value determined with the correction method was still 8.3. I_c and the n-values of the MgB_2 tape have been verified in [73] with a conduction cooled, high conductivity sample holder and with the optimum current ramp rate to be 179 A and 14, respectively.

BSCCO tape measurements

BSCCO tape measurements were carried out in measurement station where the tape was cooled down to 73 K at normal pressure using gas-flow. Helium gas was used to cool down the sample space. The needle valve set the gas flow speed after which the temperature of the gas was adjusted using a heat exchanger and heater. During the measurements, the needle valve was closed to obtain a non-cooled situation in the sample. A conceptional picture of the measurement system is shown in Fig. 5.11. The sample was wound around a sample holder made of TiAlV. Both ends of the sample were soldered to the sample holder copper ends using 97Sn3Ag solder. Finally, the voltage taps were soldered to the lead 20 cm apart from each other, and the tape was covered with a small layer of Stycast epoxy.

During the measurements, current was ramped with different rates between 2 A/s and 30 A/s. For consistency, multiple measurements were made at each ramp rate for both samples. Current was then allowed to reach approximately 10 A over the electric field criterion E_c of 1 μV/cm, after which the current was ramped down with a rate of 20 A/s. Next, the measurement curves were corrected by using the correction method. Figs. 5.12 and 5.13 show I_c and the n-value of BSCCO tape of both, ascending and descending, current ramps as well as the corrected values with various current ramps at 73 K.

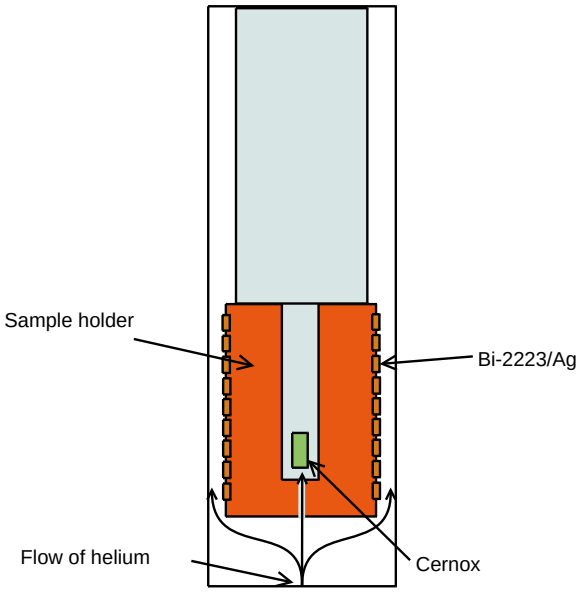

Figure 5.11: Sample holder for BSCCO tape.

Gas cooled BSCCO tape measurements showed similar behavior as the MgB_2 tape sample although deviation was reduced due to high specific heat in the TiAlV sample holder and superior thermal conductivity in the BSCCO tape. Furthermore, the TiAlV sample holder provided some cooling during the measurement, and the conditions were not completely adiabatic as the correction method assumes. Thus, in contrast to MgB_2 tape at low current ramp rates, Eq. (5.11) was giving too low I_c values and slightly too high n-values. The constant temperature I_c and the n-values of the BSCCO tape at 73 K were measured to be 147 A and 9, respectively.

5.2.3 Discussion

Although the presented correction method can be used to improve results, cooling should be made as efficient as possible during the measurements. However, when systems with low cooling power such as conduction cooled systems are used, it would be good practice, if possible, to measure both ascending and descending current ramps to verify if the temperature remains constant in

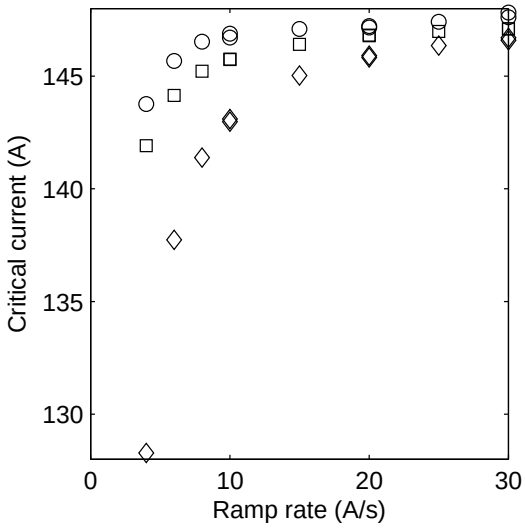

Figure 5.12: Measured I_c-values of BSCCO tape at ascending (□), descending (◇) and corrected values (○).

the sample. If deviation between the curves are found, the presented method can be used to improve the results. Furthermore, the method can be used to

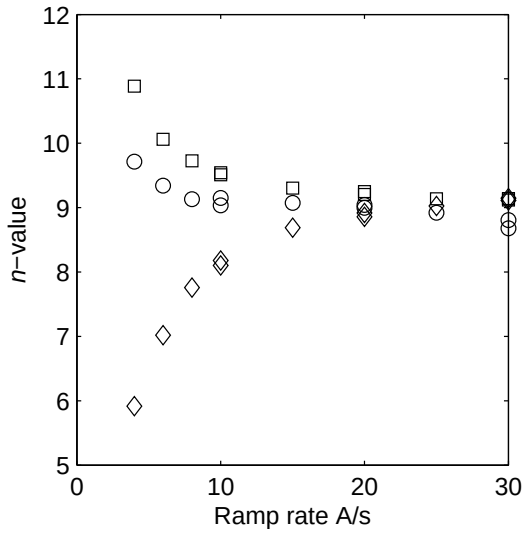

Figure 5.13: Measured n-values of BSCCO tape at ascending (□), descending (◇) and corrected values (○).

formulate constant temperature $V(I)$-curves at overcritical currents. This is important data for designing fault current limiters, especially when calculating the response time for these systems.

5.3 Conclusions

In order to better understand features of $V(I)$-curves in samples, I measured $V(I)$-curve of both BSCCO tape and MgB_2 tape in adiabatic conditions. Warming distorts the $V(I)$-curve of the sample, but the influence of heating can be compensated computationally. The presented correction method is based on the voltage data from both the ascending and descending branches of a triangular current ramp. In the presented method, adiabatic conditions and C_p independent of T were assumed. Then, the method can produce fairly well constant $V(I)$-curves even from poorly measured data.

Chapter 6

Variable current ramp in BSCCO-coil

The computational stability analysis for HTS coils at DC currents is already well established [41, 45, 78] and the understanding about electric field distribution inside HTS coils has matured [13, 62]. However, it is not yet completely clear, how the maximum stable DC operation current of the coil can be determined from the measured charging characteristics of the coil although some rules of the thumb have been proposed [32, 40]. Data presented in this chapter is based on Publication I.

In LTS coils which have high n-values and operate in liquid coolant, the measured critical current has decreased with increased ramp rate due to AC losses [2, 11, 56]. Similar behaviour has also been found in Bi-2223 tapes [24]. However, in HTS coils the analysis of AC losses during a coil charging has not been carried out so far. In this section, a stability model which takes into account AC losses is developed. The model is used to simulate the charging characteristics in a high quality Bi-2223/Ag coil.

6.1 Bi-2223 coil

Here a solenoidal coil wound of Bi-2223 tape was investigated. The tape used was in the coil was older version Bi-2223/Ag tape presented earlier and should not be mixed to BSCCO tape. The Bi-2223 magnet has inside and outside diameters of 255 mm and 319 mm, respectively. Coil was originally prepared by stacking 11 double pancake coils, joining the pancakes with low-resistivity joints, and vacuum impregnating the coil with epoxy resin. However, over the years it was damaged and one pancake had to be removed from between, and thus now, the coil consisted of 10 pancakes. Three tapes, having dimensions of 0.18 mm x 2.60 mm per tape, were connected in parallel and wound to double pancakes. The dimensions of the coil are shown in Fig. 6.1, the length of the tape in the coil was 941 m and the corresponding coil inductance L was 0.4 H [61].

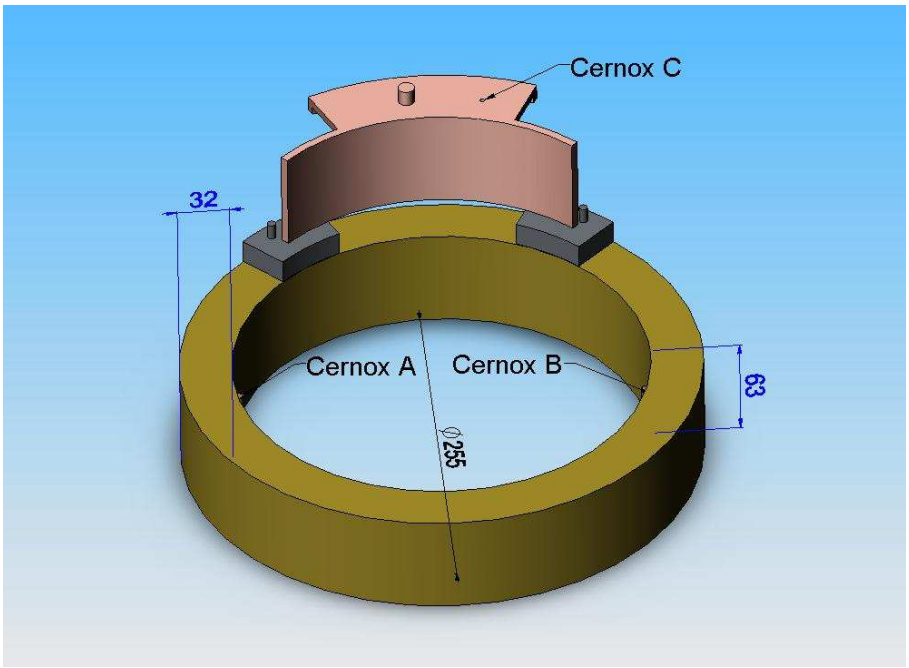

Figure 6.1: Geometry and dimensions of coil.

A two stage Gifford-McMahon cryocooler with the cooling power of 7 W at 20 K and 50 W at 80 K was used to cool down the coil and copper radiation shield. Two Bakelite plates were used to tighten the thermal interface to the coil. The interface was sliced into four separate sections to reduce eddy current losses as shown in Fig. 6.2. Each section was cooled via a hydrogen heat pipe from the second stage of the cryocooler. A heater fixed in the second stage regulated the cooling power and thereby controlled the temperature of the coil. HTS current leads were also used to reduce the heat flux in the coil. The coil system is described in detail in [61].

6.2 Computational model

In order to better understand the stability and quench behavior of the HTS coil during the charging of the coil, a numerical stability model which takes into account the losses due to the changing magnetic field was created. The model is based on the heat conduction equation

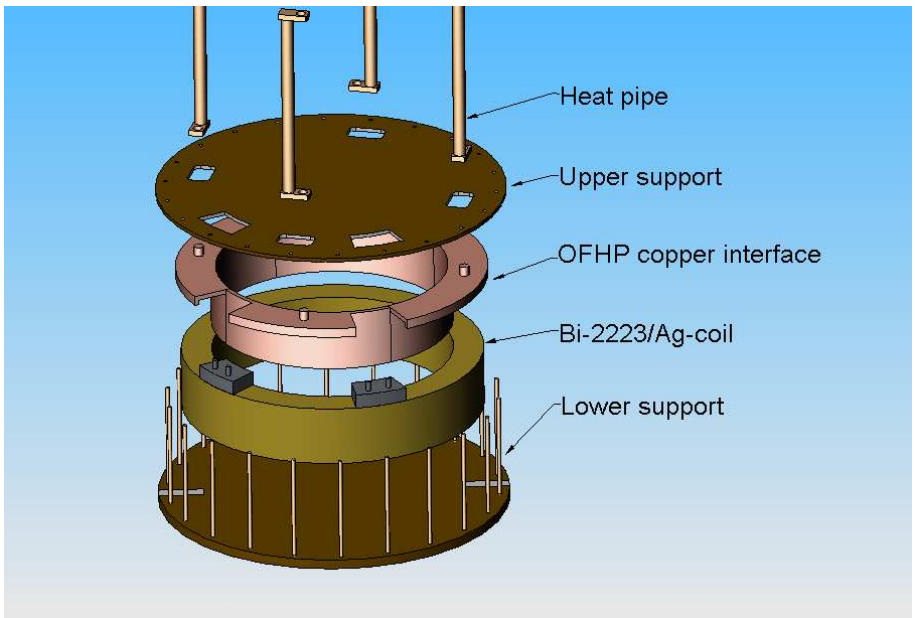

Figure 6.2: Overview of coil system.

$$\nabla \cdot \lambda(T)\nabla T + p(T) = C_{\mathrm{p}}\frac{\mathrm{d}T}{\mathrm{d}t}, \tag{6.1}$$

where p the volumetric heat generation power and C_{p} the volumetric specific heat. Equation (6.1) was solved with the finite element method. Since the used numerical model for stability considerations in HTS coils at DC currents is presented in detail in [45, 61]. I concentrate here on how to model losses created by changing magnetic fields.

Hemmi et al. has presented a model to combine the heat conduction equation with Maxwell's equations in HTS tapes carrying transport current [24]. However, this model cannot be conveniently applied on the coils because then the electromagnetic boundary conditions should be defined on the surface of each turn. Therefore, the heat conduction equation was not combined directly with Maxwell's equations but the heat generation was solved separately.

In superconducting systems losses arise due to the current in the conductor and due to the external magnetic field. In practice, these self-field and magnetization losses cannot be distinguished from each other but it is a widely used approximation to divide heat generation into two parts as

$$p = p_{\mathrm{self}} + p_{\mathrm{mag}}, \tag{6.2}$$

where p_{self} is the self field loss and p_{mag} the magnetization loss.

Here it was assumed that the changes in the self-field are small if compared to the changes in the external field. Then the self-field losses consist only of resistive losses due to the slanted $E(J)$ characteristic. I use the power law approximation 2.2. Then the self field loss can be given as

$$p_{\mathrm{self}} = \beta E_{\mathrm{c}}\left(\frac{J^{n+1}}{J_{\mathrm{c}}^{n}}\right). \tag{6.3}$$

where β is the volumetric fraction of the superconductor in the coil. Next, I calculate the penetration field B_{p} for the tape. According to the Bean model the penetration field is

$$B_{\mathrm{p}} = a\mu_0 J_{\mathrm{c}} \tag{6.4}$$

where a is half of the tape thickness and μ_0 the permeability of the vacuum. The equation estimates that the B_p is 53 mT. Thus, magnetic flux (B) exceeds the B_p in all tapes when the current is higher than 5 A. Therefore constant $\mathbf{B} = \mu_0\mathbf{H}$ in the tape cross-section can be assumed. Next, the magnetization losses are derived following the same principle as in [4, 44]. When the field directions in Fig. 6.3 are used the average dissipated power per unit volume is

$$p_\mathrm{mag} = \frac{1}{S}\int_\mathrm{S} \frac{\beta J_\mathrm{c} E^{1+1/n}}{E_\mathrm{c}^{1/n}} \mathrm{d}s = \frac{\beta J_\mathrm{c}}{S E_\mathrm{c}^{1/n}} \int_\mathrm{S} \left| x\dot{B} \right|^{1+1/n} \mathrm{d}s. \tag{6.5}$$

where S is the area of filamentary region and n the index number of the conductor. Here current ramps $I(t) = I_\mathrm{r}t$, where I_r is the ramp rate, are studied. During a ramp the current creates the magnetic flux density $B(t) = B_1 I(t) = B_1 I_\mathrm{r} t$, where B_1 is the magnetic flux density at a current of 1 A. If the filamentary region inside a HTS tape is assumed to be elliptical Eq. (6.5) reduces to

$$p_\mathrm{mag} = \frac{\beta J_\mathrm{c} \left(B_1 I_\mathrm{r}\right)^{1+1/n}}{E_\mathrm{c}^{1/n}} \frac{\alpha^{2+1/n} a^{1+1/n}}{\pi} \frac{n}{3n+1} X(\alpha, n, \phi), \tag{6.6}$$

where α is the aspect ratio of the conductor, ϕ field orientation and

$$X(\alpha, n, \phi) = \int_0^{2\pi} \frac{\left|\cos(\theta)\right|^{1+1/n}}{\left[\cos^2(\theta-\phi) + \alpha^2 \sin^2(\theta-\phi)\right]^{(3n+1)/2n}} \mathrm{d}\theta \tag{6.7}$$

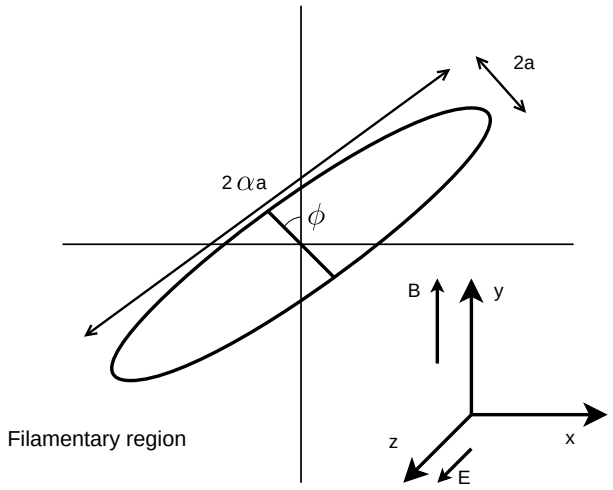

Figure 6.3: Geometry of filamentary region in a tape and field directions.

is evaluated numerically.

In practice both J_c and n depend on $\mathbf{B}$, and thereby, vary during the current ramp. The $J_c(\mathbf{B})$ and $n(\mathbf{B})$ data used here is presented in detail in Publication I.

In the normal conducting interface eddy current losses P_{ed} were calculated from

$$P_{ed} = \frac{K_{ed}}{\rho_{Cu}(B,T)} \left(\frac{dI}{dt}\right)^2, \tag{6.8}$$

where K_{ed} is a geometry dependent factor calculated using 3d FEM and ρ_{Cu} the electrical resistivity of copper [37]. Adiabatic situation was assumed in the boundaries and no radiation was taken into account. Only cooling to the coil came from the top copper interface.

6.3 Results and discussion

It is well known that for short times HTS coils can be operated at overcritical currents, but appropriate quench protection methods have been difficult to design. On the other hand, from the measured charging characteristics it has been problematic to find out if there are defects like resistive joints inside a HTS coil. The method presented in this paper can help to design a protection scheme for overload conditions. However, this paper concentrates only on the very basic relations between the measured voltage current characteristics and the real coil behavior. The understanding about these relations is needed before applications like protection systems can be developed.

Two widely used design criteria for HTS coils using the DC current are, I_s at which the thermal runaway occurs and the average electric field E_c inside the coil at a constant temperature. Previously it has been suggested that an average electric field of 0.1 μV/cm is an appropriate estimate about the stable DC operation current for Bi-2223/Ag coils at 20 K [40]. When the operation temperature rises, E_c can be increased as well. Here $I_s(20\,\mathrm{K})$ and $I_s(45\,\mathrm{K})$ were 228 A and 148 A, respectively. This was in good agreement with the before

mentioned rule of thumb because at 20 K I_s corresponded to E_c of 0.1 $\mu V\text{cm}^{-1}$ and at 45 K to about 0.3 $\mu V\text{cm}^{-1}$.

Next these two basic design criteria were compared with computed critical currents taking into account cooling and losses at different ramp rates. With $E_c = 0.1$ $\mu V\text{cm}^{-1}$ criterion at 45 K the critical currents were within 5% from the value computed at a constant coil temperature. Otherwise the maximum difference was about 10%. It was also found at both temperatures that at $E_c = 1$ $\mu V\text{cm}^{-1}$ there was a local maximum of I_c in the studied interval of ramp rates. This phenomenon is depicted more clearly in Fig. 6.4. At lower current ramp rate the coil has more time to warm up due to the resistive losses yielding to lower I_c. With higher current ramp magnetization and eddy current losses dominate leading to decreased I_c. Somewhere in between all losses are minimized and an optimum is found. It is also seen that at 20 K and $E_c = 0.1$ $\mu V\text{cm}^{-1}$ the local maximum was achieved at the ramp rate of 0.1 As^{-1}.

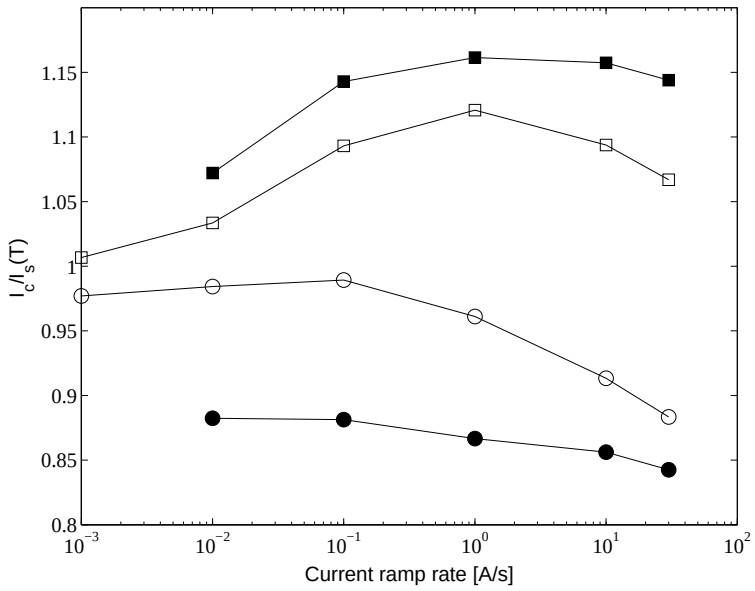

Figure 6.4: Normalized critical currents $I_c/I_s(T)$ as a function of ramp rate. Curves correspond to operation temperatures and electric field criterions of (○) 0.1 μVcm^{-1}, 20 K; (□) 1 μVcm^{-1}, 20 K; (●) 0.1 μVcm^{-1}, 45 K; (■) 1 μVcm^{-1}, 45 K; . Stability currents are $I_s(20K) = 228$ A and $I_s(45K) = 148$ A.

In each case the maximum I_c was within 1% of the critical current computed at the constant temperature. This result suggests that the maximum stable DC operation current can be estimated from the measured voltage current characteristics as a maximum critical current at the temperature dependent electric field criterion given in [37].

Computations can be further exploited to distinguish the relative importance of different loss components. Fig 6.5 shows how the magnetization losses dominate when the ramp of 10 As^{-1} was used while with $\mathrm{d}I/\mathrm{d}t = 1$ As^{-1} the I_c was determined by the resistive losses. Since the current ramp rate was kept constant and the critical current density decreased as a function of current, the magnetization losses diminished as the current increased.

6.4 Conclusions

I created a numerical stability model which takes into account both resistive transport current losses due to the slanted $E(J)$-curve and magnetization losses due to the changing magnetic field in the coil. The model was applied on coil

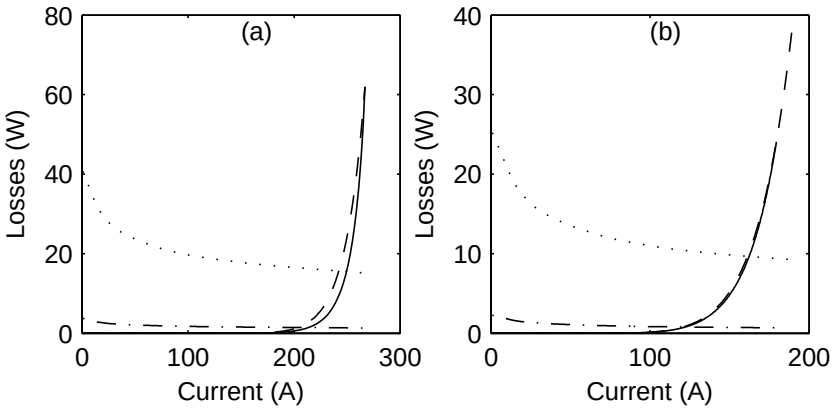

Figure 6.5: Computed losses in Bi-2223/Ag coil (a) at 20 K and (b) at 45 K: (solid line) transport current losses 1.0 As^{-1}; (dashed line) transport current losses 10 As^{-1}; (dash-dotted line) magnetization losses 1.0 As^{-1}; and (dotted line) magnetization losses, 10 As^{-1}.

wound out of BSCCO tape with similar construction as used in a HTS μ-SMES built at TUT. The simulations suggested that the coil critical currents determined with the 1 μVcm^{-1} criterion at 20 - 45 K or with 0.1 μVcm^{-1} at 20 K have a local maximum with respect to the current ramp rate used in the measurement. These maxima are found in the range 0.1 - 1 As^{-1}, and they can be used to estimate limits for the stable DC operation current of the coil.

Chapter 7

Cryogenic Design of Aluheat Project

Conventional induction heaters have relatively low efficiency due to the losses in heating coils. Such heaters are used at extrusion plants around the world to preheat aluminium, copper, and other metallic billets before extrusion to profiles. The power ratings may exceed 1 MW, and the energy efficiency is only 45 - 60% for heaters in use today. The large losses appear in the hollow, water-cooled copper conductors of the coil surrounding the billet which generate an AC current inducing currents in the billet [52]. Data presented in this chapter is based on Publications III and VII.

The Aluheat project aims at building a cryogen-free superconducting induction heater. Superconducting induction heaters generate no losses in the coils, and thus, reduce the losses to one fifth [36]. In this chapter, the concept behind the Aluheat project is explained in detail, and the main design is presented. First, I present the original design including coil design and cryogenics. The last section deals with implemented changes and improvements needed later during the project.

7.1 System overview

An aluminum billet was placed between two parallel disc-shaped cryostats each having the diameter of 1.6 m and the thickness of 0.5 m. One Gifford-McMahon cryocooler with the cooling power of 15 W @ 20 K and 80 W @ 80 K cools down each cryostat. The decagonal copper radiation shield having an RRR of 100 was composed of two end plates and ten similar plates on the sides as shown in Fig. 7.1. Both the radiation shield and the coil hang from a steel plate attached to the cryostat top. The interface of the coil having an RRR of 250, and it will be assembled as mechanically flexible comb like structure that ensures good thermal homogeneity over the coil and reduces eddy current losses during ramping. A small gap is left at both sides between the interface and the coil due to differences in thermal contraction. The combs of the interface will be attached to the coil with Stycast 2850-FT epoxy resin. All the thermal contacts, which do not need to be electrically insulated, will be copper-copper pressure joints with Apiezon N grease between the surfaces. Electrically insulated contacts are achieved using thin layers of fiberglass rubber on both surfaces and Apiezon N grease between the contacts. Since the coils are very close to each other they must be supported against horizontal magnetic force which pulls them together. Therefore, the bakelite cage was designed to surround the coil fixed to the cryostat walls using G-10 epoxy-fiberglass tubes. Later the bake-

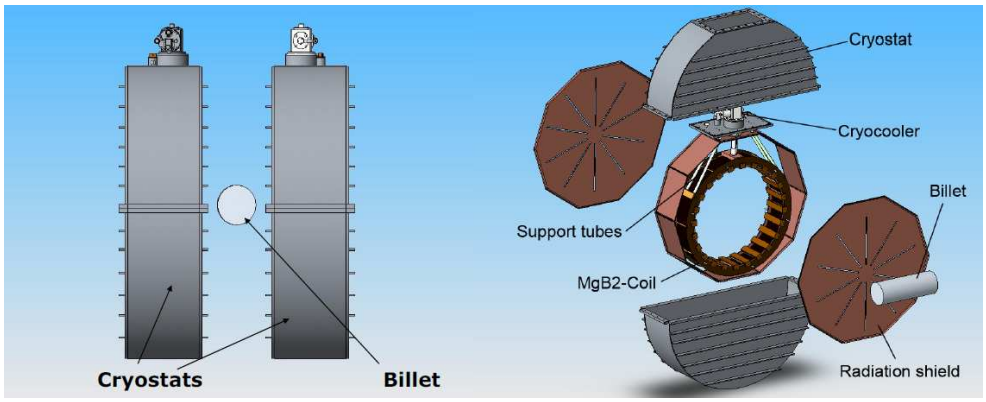

Figure 7.1: Structure of one disc-shaped cryostat

lite cage was left out of the design and supporting epoxy-fiberglass tubes were fixed straight to the interface. Furthermore, extra bakelite support rings were added to prevent the deformation of the radiation shield due to the Lorentz forces in case of a quench.

7.2 Design of the Aluheat project

Depending on a cryostat to be designed, properties needed to be taken into account vary. When a superconducting induction heater cryostat was designed important aspects included heat loss minimization, mechanical analysis against vacuum forces, securing the coil into place to prevent any movement and assembling such a large system in a small laboratory.

7.2.1 Manufacturing of coil

The design of a coil system depends on the requirements of the particular heater. Dimensions of the billet to be heated, mechanical system of the heater and desired temperature profiles set the frames, whereas conductor properties and chosen coil winding technique determine the final shape of the coil. The coil system outlined here was designed for billets with the diameter of 215 mm and with lengths up to 700 mm. The magnetic field was generated by a Helmholtz configuration of two vertically mounted superconducting coils which were located at a distance of about 800 mm. For necessary heating power, the magnetic field over the billet was about 0.5 T @ 200 A, depending somewhat on the angular velocity chosen for the billet rotation. The magnetic field at the inner surface of the coils is approximately 1.7 T. When the billet was placed between the cryostats the magnetic field was oriented in perpendicular to the billet axis as shown in Fig. 7.2. The use of MgB_2 superconductors makes the coil design flexible in terms of conductor length. MgB_2 superconductors are relatively inexpensive, and as the coil operates in DC, additional conductor length does not yield noteworthy-additional energy losses. In this

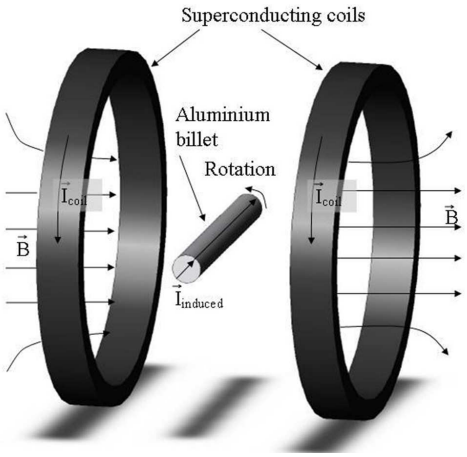

Figure 7.2: Billet is placed between the cryostats and rotated for the heating.

investigation, the coils had an outer diameter of 1100 mm, thickness of 50 mm and the height of 180 mm as presented in Fig. 7.3. Approximately 8.8 km of MgB2 superconductor tape is used for one coil, the number of turns is 2400 and the inductance 4.9 H [53].

Each coil was built of 16 double pancake coils, with joints on the outer side. The MgB_2 tape was first insulated with a 25 μm thick Kapton foil. Then the pancakes were wound with a wet layer technique using Stycast 2850-FT. Afterwards they were stacked together and reinforced with epoxy impregnated glass-fibre tapes. The current in the coils, and hence the magnetic field, depends somewhat on the particular billet to be heated. A typical value of the magnetic field was about 0.5 T in the centre of the billet at rest, and the coils themselves were exposed to the magnetic field of about 1.6 T at the corners closest to the billet.

Insulation

Insulation of the tape and manufacturing of the coil was performed in SINTEF in Norway. In principle, wet winding will provide electrical insulation between the adjacent conductor layers by the epoxy used. However, to ensure insulation also for parts of the superconductor possibly not entirely covered by epoxy,

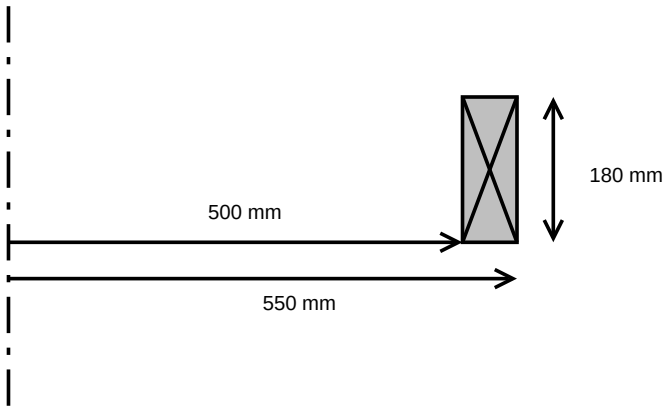

Figure 7.3: MgB_2 coil dimensions

a polyimide film (Kapton tape) was, prior to the coil winding, applied to the superconductor using a specially designed machine shown in the Fig. 7.4. The polyimide film (25 μm thick, 8 mm wide, and with glue on one side) was rolled onto the back side of the conductor and then wrapped around the conductor using rubber rolls leaving an approximately 2 mm strip on the front

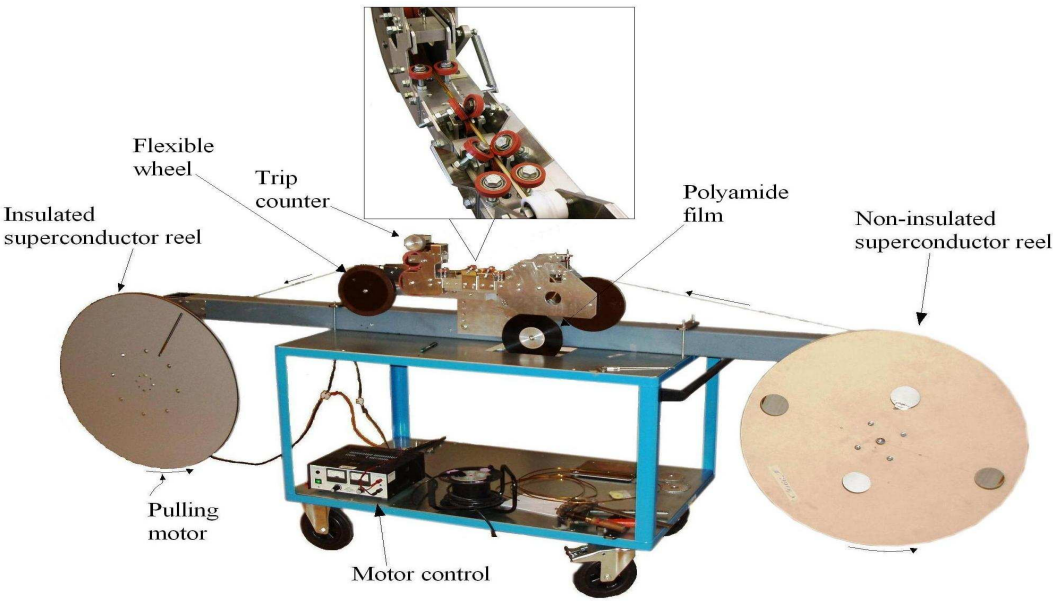

Figure 7.4: Insulation machine with rubber rolls for tape wrapping in the inset. Courtesy of the SINTEF energy research center in Norway.

side uncovered. The guiding wheels of the insulating machine had all radii greater than the minimum bending radius of the superconductor, i.e. 100 mm or more. The machine was also designed such that the superconductor was never bended in the direction opposite to its original bending direction. The machine was equipped with an adjustable motor speed drive which pulled the superconductor through the insulating procedure of the rubber rolls and on to a reel.

The insulating machine was successfully tested for operation speeds up to 20 m/min. However, when insulating the tape for the coil, a speed of typically 12 - 15 m/min was used. The insulation system was operated by one person.

Wet winding

After insulating the tape, the winding of the double pancakes was initiated. A wet winding process was chosen. In this process a layer of epoxy is continuously applied to both sides of the tape just before the tape is wound into pancakes. Hence, between every turn of the coil there will be epoxy and there is no need for vacuum impregnation after winding. From experience with dry winding processes it is well-known that it may be very difficult to ensure epoxy penetration everywhere in between the conductor layers.

Stycast 2850-FT epoxy with Catalyst 24LV as hardener agent was used. Stycast 2850-FT has a high content of alumina filler improving the thermal conductivity, and reducing the thermal contraction to close to that of metals. The pancakes were wound on to a horizontally aligned turning table shown in the Fig. 7.5. The same motor drive as during the insulating process was used to provide the pulling force. At the other end of the machine, about 3 m away, was the reel of insulated superconductor. The same precautions as in the insulating process, regarding pulling and bending of the superconductor as well as the use of a breaking mechanism for the reel with insulated superconductor, was taken. The surface of the table and the inner structure were equipped with Teflon sheaths, greased with a release agent to facilitate the release of the

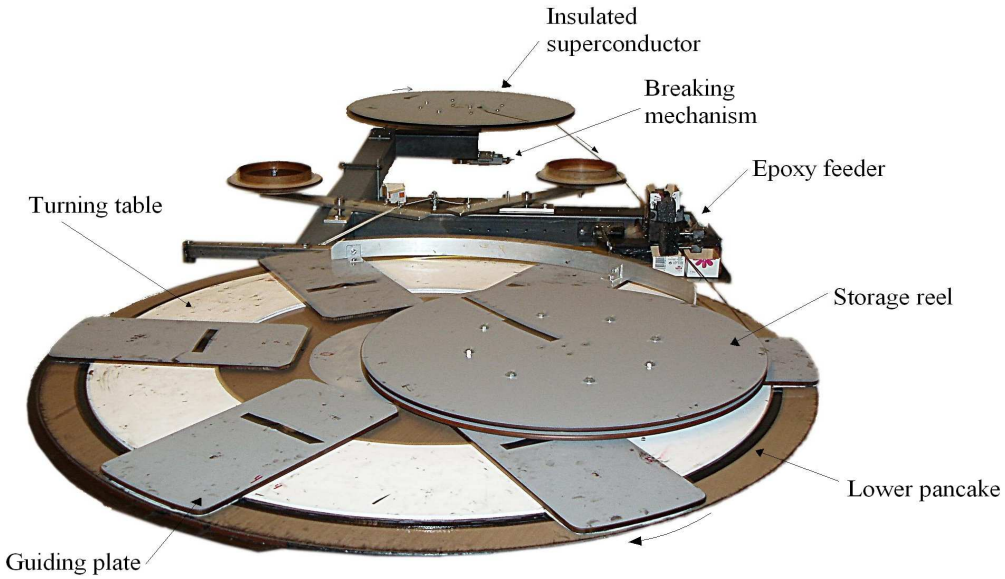

Figure 7.5: Rotating table used for wet winding of double pancakes. Winding of the lower layer with tape delivered from the reel in the back has just begun. The storage reel on top of the rotating table contains the tape for the upper pancake. Courtesy of the SINTEF energy research center in Norway.

coil after curing of the epoxy.

During winding, the epoxy was applied by pulling the tape through an epoxy bath contained in a cardboard box. Excessive epoxy was wiped off with rubber wipes on each side of the tape. The thickness of the epoxy layer was controlled by adjusting the pressure of these wipes, and the following two rolls made of rubber foam distributed the epoxy evenly on the tape surfaces and edges. The cardboard container and rubber rolls were disposable, but the rest of the equipment had to be cleaned after each use. In total 32 double pan-cake coils were wound.

Stacking of the pancakes

To create one coil, 16 double pan-cake coils were stacked on top of each other. The same epoxy as used in the wet winding process was used to fix the double pan-cake coils to each other and to the cooling interface. The double pan-cake

coils were then connected in series by soldering the conductor end of one double pan-cake coil to the end of the next.

Good joints between the double pan-cake coils are crucial to avoid heating and a following reduction in critical current or in worst case a quench. Tests were performed in advance to secure a reliable and repeatable soldering technique. A 100 mm overlap joint was selected for its practical feasibility and for satisfying test results. The joints between the double pancakes were cooled by covering them with epoxy and molding them to a 10 mm x 155 mm x 580 mm copper plate which connected them thermally to the cold head. A proper cooling of the overlap joints was crucial to avoid a significant temperature rise in the superconductor due to the heat generated in the resistive overlap joints.

7.2.2 Heat losses

The coil is in a vacuum, and therefore, heat is transferred into the system only by conduction and radiation. The radiation shield and multilayer insulation reduce the heat flux P_{r} radiated from the outer cryostat wall to the coil. The radiated heat fluxes coming to the radiation shield and to the coil were calculated with analytical formulas from [31]. Furthermore, the influence of the multilayer insulation on the radiated heat was taken into account as

$$P_{\mathrm{r,rs}}(N_{\mathrm{l}}) = P_{\mathrm{r,rs}}(0)/(N_{\mathrm{l}} + 1), \tag{7.1}$$

where N_{l} is the number of multi-insulation layers (MLI) and $P_{\mathrm{r,rs}}$ the heat radiated to the radiation shield from the outer cryostat wall. In this case, 30 layers of MLI were used as a compromise which decreased the thermal radiation to the acceptable level but kept the distance between the coil and the billet short. The G-10-epoxy support tubes will be constructed of two parts. The length of the first part from the top of the cryostat to the radiation shield was 62 mm, and the length of the second part from the radiation shield to the coil was 510 mm. In the parts, the inner and outer diameters were 14 mm and 20 mm, respectively, yielding a cross-section of 1.60 cm^2 per tube.

The heat flux, P_s, conducted from the room temperature to 20 K via the four supporting G-10-epoxy tubes was solved from 1D heat transfer Eq. 3.1 with Finite Element Method (FEM). Temperature dependent thermal conductivity of the G-10 tubes was obtained from Ref. [54]. The current leads were designed to operate at 250 A in such a way that the sum of conductive and ohmic losses, P_l, in the lead was minimized. In the normal conducting part, the optimal value for the ratio IL/A, where I is the current, L the length and A the cross-section of the lead, can be derived from Ref. [26]. For brass leads, the optimal IL/A ratio was $6.5{\cdot}10^5$ A/m and for copper leads $3.5{\cdot}10^6$ A/m. Since the distance between the radiation shield and the cryostat was only 67 mm, the optimal diameter of round copper wire at 250 A would only be 2.4 mm. The small cross section is difficult to construct and is more vulnerable under over-currents. The optimal diameter for brass lead was 6 mm, and thus, brass was chosen as the material for the normal conducting part whereas commercial YBCO leads were used in the second part. The diameter of these YBCO leads was 11 mm, and their conductive heat leak was 130 mW per pair. Summary of all loss components is shown in Table 7.1.

7.2.3 Mechanical analysis

The system consisted of two 1.7 T superconducting coils very close to each other. Forces affecting the system are shown in the Fig. 7.6. $\mathbf{F}_{st}$ is the force affecting the cryostats when the billet does not rotate but the operation current is switched on. This is the worst case scenario since when the billet starts to

Table 7.1: Heat losses to the system

Loss component	To radiation shield	To coil
Radiated heat, P_r*	10 W	2 W
Losses in current leads, P_l	16 W	0.1 W
Conduction via supports, P_s	5 W	0.4 W
Pancake resistive joints	0 W	$\approx$ 1 W
Total	31 W	3.5 W

* with 30 layers of superinsulation

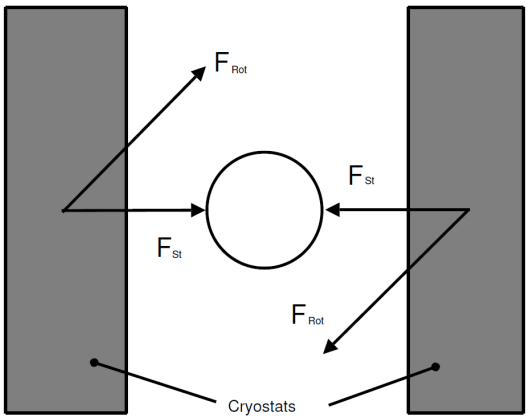

Figure 7.6: Forces affecting the cryostats with and without a rotating billet.

rotate it experiences a changing magnetic field and eddy currents are induced. Then, the magnetic flux distribution of the system changes, and therefore, the force turns and its magnitude drops significantly. Force $\mathbf{F}_{\mathrm{st}}$ was calculated by integrating the Lorenz force over the cross section of the coil to be 31 kN at normal operation conditions. The magnitude and the direction of the force $\mathbf{F}_{\mathrm{rot}}$ during the billet rotation was calculated in an infinitely long racetrack coil with 2d FEM. In the case of a solenoid direction of the $\mathbf{F}_{\mathrm{rot}}$ will be the same and the magnitude much smaller compared to $\mathbf{F}_{\mathrm{st}}$. Therefore, the worst case is when the billet is not rotated while the coils are energized. Due to the electromagnetic forces, a coil support has to be fixed to the broad sides of the cryostat to prevent movement during operation. This was achieved with six G-10 epoxy fiberglass tubes at both sides of the coil. Also large vacuum forces affect the broad sides of the cryostat, and thus, massive supports are needed to prevent it from deforming. Corresponding strain can be calculated when material properties are known. The broad sides were designed to withstand the vacuum forces with a safety factor of two. The designed broad side plates were 18 mm thick and had 30 mm high support steel bars welded to them.

7.2.4 Implemented changes

The cryostat was assembled as designed except some improvements presented below. First, to improve the mechanical stability and to restrict the movement of the coil, G-10 support tubes were replaced by a G-11 fiberglass/epoxy plate sawn to a tooth shape as shown in the Fig. 7.7. The coil was also fixed to the radiation shield using six G-11 fiberglass rods on both sides of the coil.

Using the same rods, the radiation shield was further fixed to the inner walls of the cryostat. While vacuum testing the cryostat sides began to deform and thus, stainless steel tube was added at the centre of the cryostat to further reinforce the sides against the inward vacuum forces. Secondly, during the construction, copper plate was more easily available than brass and thus, the upper part of the current leads were made of copper. Leads were first cut to shape after which I filed them to optimum width. Optimized copper leads

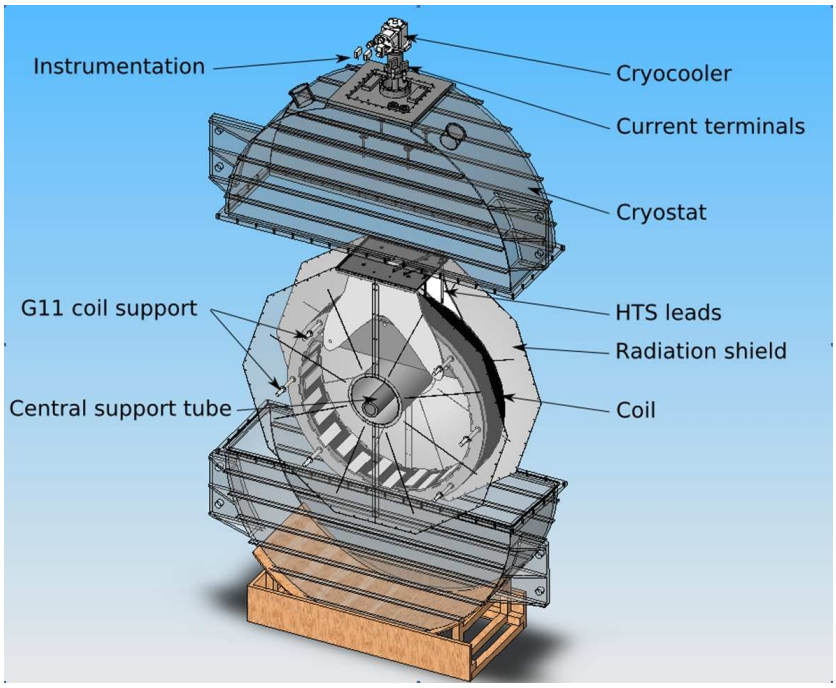

Figure 7.7: Coil was hung from G-11 fiberglass/epoxy plates which prevent movement of the coil to any direction. The stainless steel tube at the centre of the cryostat was to reinforce the sides against the vacuum forces.

are shown in Fig. 7.8, and the picture of assembly is shown in Fig. 7.9. Third, wounded coils had an inner diameter of 1.1 m, a height of 150 mm, and a thickness of 70 mm in the radial direction. Finally, YBCO current leads were changed to Bi-2223/Ag leads.

7.2.5 Cooldown tests

At precooling tests without a coil in place, temperatures in the radiation shield and in the coil were around 38 K and 7 K, respectively. The measured temperature difference between the top and bottom side of the interface was 0.4 K. The cool down time of the cryostat without the coil is presented in Fig. 7.10. Later cooling tests with the coil showed the same results except the temperature difference between the top and bottom side of the interface was around 2 K. However, for unknown reason the temperature in final tests at the top of the HTS current leads was risen around 80 K which prevented the testing with 200 A current. Nevertheless, system was tested with 185 A current and no heat generation was observed in the coil.

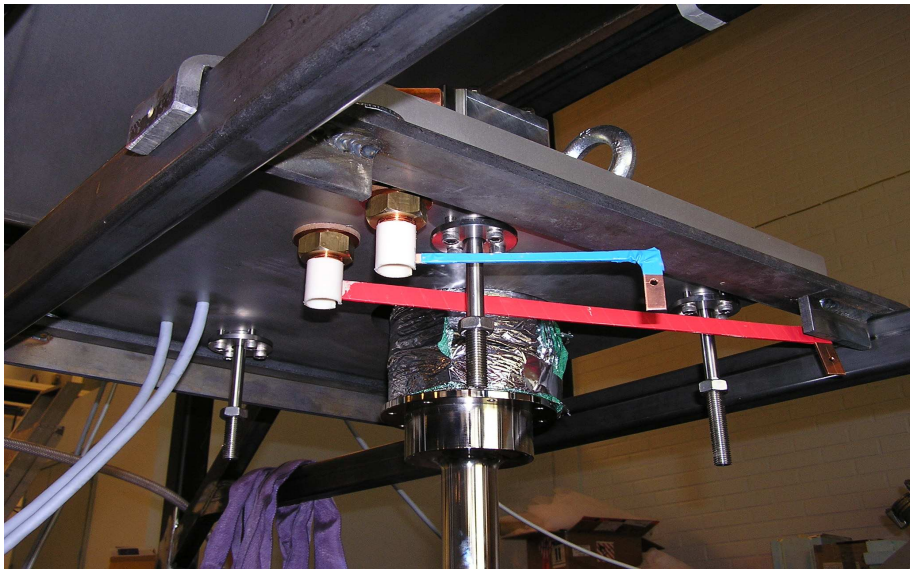

Figure 7.8: Copper current leads were filed to the optimum width. Red current lead is longer and thus, wider.

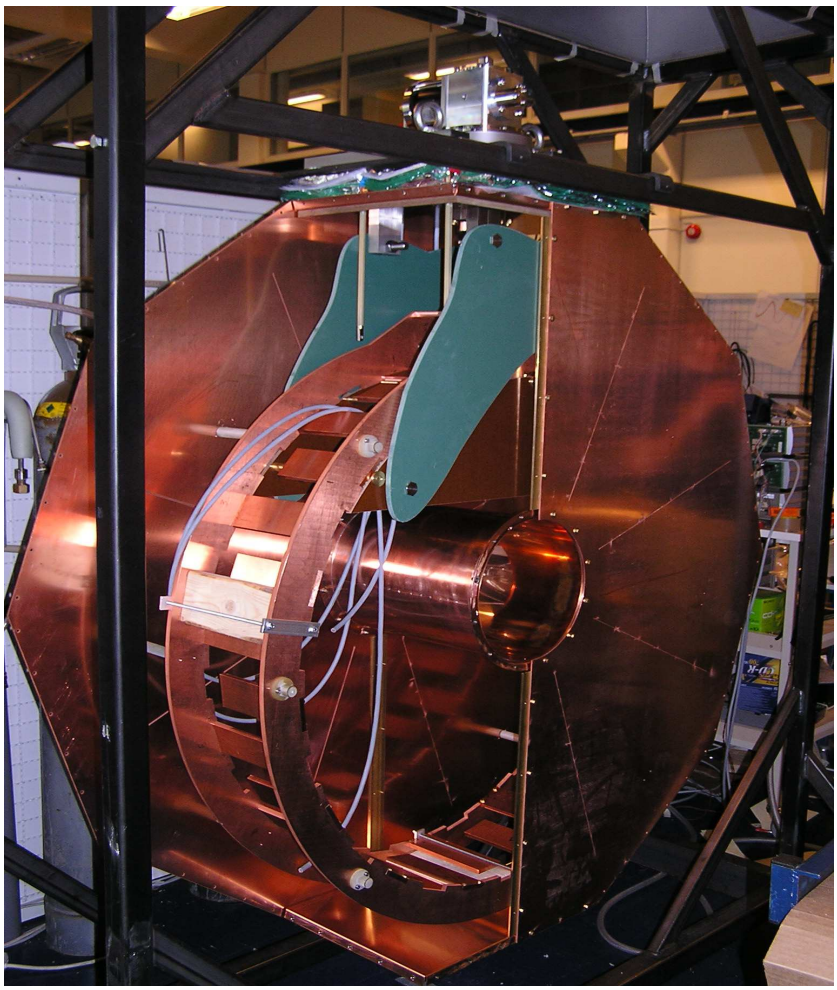

Figure 7.9: Picture of assembly.

7.3 Conclusions

In this chapter, I presented the cryogenic design of superconducting induction heater. The billet to be heated was placed between two disc shaped cryostats and rotated in an inhomogeneous magnetic field to achieve the heating effect. A superconducting heater is expected to considerably reduce the costs of heating due to the poor efficiency of the conventional heater. When the billet is rotated, the eddy currents are generated at the billet. The higher the rotational speed, the faster the heating. Unfortunately new problems arise

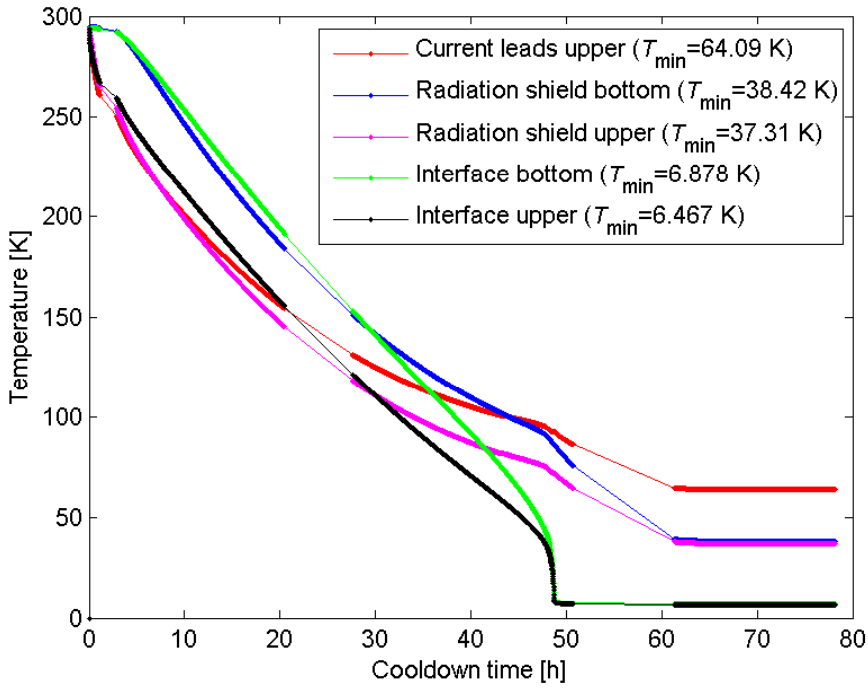

Figure 7.10: Temperature during the first cooldown test.

with the higher rotation speed and therefore a steady-state rotational speed of about 3000 rpm was selected. The system consisted of two coils close to each other, and thereby, large forces tended to pull them together. Special G-11 epoxy supports fixed between the coil and the cryostat walls were used to keep it in place. Also the vacuum forces affecting inward at the broad sides of the cryostats are large, and therefore, steel support were designed to reinforce the sides. At cooling tests temperatures in the radiation shield and in the coil were around 38 K and 7 K. The cryostats exceeded the design values and coil were tested at 185 A without significant heat generation.

Chapter 8

Conclusions

This thesis studied the cryogenic design of a superconducting induction heater in the Aluheat project and presented some tools and simulation models needed. First, I introduced the physical background of concepts used in this thesis. Next, I studied some important parameters which are needed to estimate the performance of a cryogenic system. To evaluate the coil stability and to simulate quench, the transverse thermal conductivity of the MgB_2 coil was measured and simulated. The measurements and simulations confirmed that the thermal conductivity was around four times higher, parallel to the broad side of the tape than to the perpendicular direction. Simulation also showed that only when the fill factor for the whole conductor exceeded 80% tape materials started significantly influence effective thermal conductivity of the coil. With lower fill factors, the thermal conductivity of epoxy was the determining factor.

Also, self-made current leads were studied to determine the contact resistance, thermal resistance, thermal conductivity and losses in current leads manufactured using different solders. Performance of the HTS current leads, was also evaluated by measuring properties of self-made current leads manufactured using different solders. The current lead soldered using 99.3Sn/0.7Cu was chosen due to good combination of electrical, thermal and mechanical properties.

Furthermore, I examined the behavior of voltage current characteristics in

superconducting short samples cooled with a conduction cooled system and with gas-flow measurement station. To take into account the warming of the sample, I presented a computational correction method to improve $V(I)$-characteristics which was tested for two superconducting tapes. Results show that, not only, the correction method can be used to improve poorly measured characteristics, but it can also be used to define voltage current characteristics at overcritical currents which would be impossible by any other means. However, assuming that specific heat does not depend on temperature leads to a slight error in the results. In addition to short sample studies, a superconducting coil was also simulated with different current ramp rates to estimate the safe operating current in the coil. A model taking into account both resistive transport current losses as well as magnetization losses due to the changing magnetic field in the coil was developed. According to the results, the critical current of the coil has a local maximum with respect to the current ramp rate used in the measurement. This maximal critical current can be used to estimate the limits for the stable DC operation current of the coil.

Finally, the cryogenic design of the Aluheat project was presented. In conventional heaters, efficiency is around 55% when heating high conductivity materials like aluminum or copper. Superconducting heaters generate no losses and, thereby, work at improved efficiency. The challenging parts of the design were to minimize the gap between the coil and the billet and to reinforce the cryostat outer walls which are exposed to huge vacuum forces. Two cryostats were assembled and preliminary test made. More extensive tests with coil inside was performed later in the summer of 2010.

This thesis studied some design issues faced during the Aluheat project. Better understanding of the material properties as well as characterization of short samples and coils helps us to improve simulation models. Application specific cryogenic design issues we faced during the project are typical problems for superconducting induction heaters and can be used as a foundation for developing the second generation heaters. However, more extensive studies about increasing thermal conductivity inside the coil as well as evening out

hot spots as needed to improve the stability of superconducting coils. In addition, the method of acquiring absolute constant temperature voltage current characteristics would standardize the measurement process and improve the bench-marking of superconducting samples.

Bibliography

[1] Ahoranta M, Bukva P, Kovac P, Mikkonen R and Tarhasaari T, "Estimation of the stress state of axially tensioned Bi-2223/Ag tapes", *Physica C* **432** 239-249, 2005.

[2] Andreev N, Arkan T, Bossert R, Brandt J, Chichili D, DiMarco J, Feher S, Kerby J, Lamm M J, Limon P J, Nobrega F, Orris D, Novitski I, Ozelis J P, Peterson T, Sabbi F, Schlabach P, Strait J, Tartaglia M, Tompkins J C, Yadav S, Zlobin A V, Caspi S, McInturff A D, Scanlan R M and Ghosh A, *Particle Accelerator Conference, Proceedings of the 1999* **5** 3197, 1999

[3] Application note, "Bonding non-metallic materials using indium and high indium alloys", http://www.indium.com, August 2007

[4] Banno N, Amemiya N, Mihoichi A, Ciszek M, Mukai H and Ohmatsu K *IEEE Trans. Appl. Supercond.* **9** 2565, 1998

[5] Biocca P, "Global Update on Lead-free Solders" *Proc. Surface Mount International (San Jose, CA)*, 705-709, 1998

[6] Bogdanov I, Kozub S, Myznikov K, Slabodchikov P, Sychev V, Sytnik V, L. Vassiliev L, Zubko V, Akimov I, Gryaznov N, Rakov D, Shikov A, "Application of hts bi-2223 for current leads of superconducting magnets" *Proceedings of EPAC (Vienna, Austria, 2000)*

[7] Collocot S.J., Driver R, Andrikis C. "Specific heat of the ceramic superconductor Bi2Sr2CuO6 from 0.4 to 20 K", *Physica C* **173** 117-124, 1991

[8] Cryogenic temperature sensors specifications, "Technical specifications", http://www.lakeshore.com, April 2009

[9] Current Leads, "CryoSaver Current leads", http://www.hts-110.com/, May 2010

[10] Database for Solder Properties with Emphasis on New Lead-free Solders Release 4.0, "Properties of Lead-Free Solders", http://www.boulder.nist.gov/.

[11] den Ouden A, Wessel S, Krooshoop E and ten Kate H *IEEE Trans. Appl. Supercond.* **7** 733, 1997

[12] Dorri B, Herd K, Laskaris E T, Tkaczyk J E and Lay K W, "High temperature superconducting current leads for cryogenic applications in moderate magnetic fields" *IEEE Trans. Magn.* **27** 1858-1860, 1991

[13] Fabbricatore P, Priano C, Testa M, Musenich R, Kováč P, Matrone A, Pertillo E and Ariante M *Supercond. Sci. Technol.* **11** 304, 1998

[14] Flükiger R, Suo H L, Musolino N, Beneduce C, Toulemonde P, Lezza P, "Superconducting properties of MgB_2 tapes and wires" *Physica C* **385** 286-305, 2003

[15] Flynn T M, "Cryogenic engineering", *Marcel Dekker*, New York, 2005

[16] Glowacki B A, Majoros M, Eisterer M, Toenies S, Weber H W, Fukutoni M, Komori K and Togano K, "MgB_2 superconductors for applications" *Physica C* **387** 153-161, 2003

[17] Goldacker W, Schlachter S I, Liu B, Obst B and Klimenko E, "Considerations on critical currents and stability of MgB_2 wires made by different preparation routes." *Physica C* **401** 80-86, 2004

[18] Goodrich L F, Bray S L, "High T_c superconductors and critical current measurements", *Cryogenics* **30** 667-676, 1990

[19] Goodrich L F, "High T_c superconductor voltage-current simulator and the pulse method of measuring critical current", *Cryogenics* **31** 720-727, 1991

[20] Gordon J.E., Prigge S, Collocot S.J., Driver R, "Specific heat of (Bi,Pb)2Sr2Ca2Cu3O10+y from 78 to 300 K", *Physica C* **185** 1351-1352, 1991

[21] Grant P M, "Superconductivity: Prospecting for an iron age" *Nature* **453** 1000-1001, 2008 doi:10.1038/4531000a

[22] Hasselman D P H, Johnson L F, "Effective thermal conductivity of composites with interfacial thermal barrier resistance" *Composite materials* **21** 508-515, 1987

[23] Heller R, Friesinger G, Fuchs A M, Mito T, Satoh S, Takahata K, Tasca M, Vogel M, "Development of a 20 kA high temperature superconductor current lead" *Cryogenics* **41** 539-547, 2001

[24] Hemmi T, Ninomiya A, Ishigohka T, Kurahashi K, Arai K, Yamaguchi H, Umeda M, and Kaiho K, *IEEE Trans. Appl. Supercond.* **12** 1422, 2002

[25] Hermann P F et al., "European project for the development of high T_c current leads" *IEEE Trans. Appl. Supercond.* **3** 876-880, 1993

[26] Hermann P F in Seeber B (edit.), "Handbook of applied superconductivity" *Institute of Physics Publishing*, 801-843, 1998, Bristol

[27] Hiltunen I, Korpela A and Mikkonen R, "Solenoidal Bi-2223/Ag induction heater for aluminium and copper billets", *IEEE Trans. Appl. Supercond.* **15** 2356, 2005

[28] Horvat J, Yeoh W K, Kim J H and Dou S X. "Transport and magnetic critical current in superconducting MgB_2 wires" *Supercon. Sci. Technol.* **21** 065003 (6pp), 2008

[29] Hull J R, "High temperature superconducting current leads for cryogenic apparatus" *Energy Conversion Engineering Conference, IECEC-89. Proceedings of the 24th Intersociety* **1989** 459-464, 1989

[30] Hull J R, "High-Temperature Superconducting Current Leads" *IEEE Trans. Appl. Supercond.* **3** 869-875, 1993

[31] Incropera F P, and Dewitt D P, "Introduction to heat transfer 3rd ed" *John Wilay & Sons*, New York, 1996

[32] Ishiyama A and Asai H *IEEE Trans. Appl. Supercond.* **11** 832, 2001

[33] Iwasa Y *Cryogenics* **18** 705, 1979

[34] Iwasa Y, "Case studies in superconducting magnets, design and operational issues", 1994, *Plenum Press*, New York and London

[35] Jones W, Liu Y, Shah M and Clarke R, "Mechanical properties of Pb/Sn, Pb/In and Sn-In solders" *Soldering & Surface Mount Technology* **10** 37-41, 1998

[36] Kellers J et al., "Magnetic billet heating rivals conventional furnaces" *Heat processing* 205-210, 2009

[37] Korpela A, Kalliohaka T, Lehtonen J, Mikkonen R, Pitel J, and Kováč P *Physica C* **372-376** 1360, 2002

[38] Korpela A, Lehtonen J, and Mikkonen R *Supercon. Sci. Technol.* **16** 1262, 2003

[39] Korpela A, Lehtonen J, and Mikkonen R, "Optimization of HTS superconducting magnetic energy storage magnet volume" *Supercon. Sci. Technol.* **16** 833, 2003

[40] Korpela A, Lehtonen J, and Mikkonen R *Supercon. Sci. Technol.* **16** 355, 2003

[41] Kiss T, Inoue M, Hasegawa K, Ogata K, Vysotsky V, Ilyin Y, Takeo M, Okamoto H and Irie F, *IEEE Trans. Appl. Supercond.* **9** 1073, 1999

[42] Larbalestier D, Gurevich, A, Feldmann M, Polyanskii A "High-T_c superconducting materials for electric power applications" *Nature* **414** 368-377, 2001

[43] Lee Y M, Haji-Sheikh A, Fletcher L S, Peterson G P "Effective thermal conductivity in multidimensional bodies" *ASME J Heat transfer.* **116** 17-27, 1994

[44] Lehtonen J, Korpela A, Paasi J, Pitel J, Kováč P *Supercond. Sci. Technol.* **12** 450, 1999

[45] Lehtonen J, Mikkonen R and Paasi J *Supercon. Sci. Technol.* **13** 251, 2000

[46] Lehtonen J, Mikkonen R and Paasi J, "Effective thermal conductivity in HTS coils" *Cryogenics* **40** 245-249, 2000.

[47] Lehtonen J, Mikkonen R and Perälä R, "Temperature dependent self-field effect in measured V (I,B)-characteristics of Bi-2223/Ag tapes", *Physica C* **401** 151-154, 2000

[48] Lide D R (editor), "CRC Handbook of Chemistry and Physics" *CRC Press* 12-136, 1993

[49] Lvovsky Y, "Index loss effect in n-value measurements of commercial superconductors", *IEEE Trans. Appl. Supercond* **19** 2313, 2009

[50] Magnetic billet heaters, "Magnetic billet heaters for non-ferrous metal extrusion", http://www.zenergypower.com, May 2010

[51] Magnusson N, Bersås R and Runde M, "Induction Heating of Aluminium Billets Using HTS DC Coils", *Physica C* 372-376, 2003

[52] Magnusson N, Bersås R and Runde M "Induction Heating of Aluminium Billets Using HTS DC Coils", *Inst. Phys. Conf. Ser.* **181** 1104-1109, 2004

[53] Magnusson N and Runde M "A 200 kW MgB_2 induction heater project", *J. Phys. Conf. Ser.* **43** 012159, 2006

[54] Marquardt E D, LE J P and Radebaugh R, "Cryogenic materials properties database", *11*$^{\text{th}}$ *International cryocooler conference*, Keystone, June 20-22, 2000

[55] Marquardt E D, Le J P and Radebaugh R, "Cryogenic material properties database" *Cryocoolers 11*, Springer US, Part: **17** 681-687, 2002

[56] McInturff A, Carson J, Engler N, Fisk H, Hantf R, Lundy R, Mantsch P, Nicol T, Niemann R, Schmidt E, Szymulanski A *IEEE Trans. Magn.* **21** 478, 1985

[57] Musenich R et al. "Behaviour of MgB2 react & wind coils above 10 K" *IEEE Trans. Appl. Supercond.* **5** 1452-1456, 2005

[58] Musenich R et al. "Behaviour of cryogen-free MgB_2 react and wind coils." *Supercond. Sci. Technol.* **19** 126-131, 2006

[59] Ogawa J, Sawai Y, Nakayama H, Tsukamoto O and Miyagi D, "n value and Jc distribution dependence of AC transport current losses in HTS conductors", *Physica C* **401** 171-175, 2004

[60] Ohsemochi K, Ono M, Nomura S, Kuriyama T, Kasahara H, Akita S and Koso S, "Development of 3kA conduction cooled HTS current lead system", *Cryogenics* **43** 643-648, 2003

[61] Paasi J, Lehtonen J, Kalliohaka T, and Mikkonen R, "Stability and quench of a HTS magnet with a hot spot", *Supercon. Sci. Technol.* **13** 949, 2000

[62] Pitel J and Kováč P *Supercond. Sci. Technol.* **10** 7, 1997

[63] Rogacki K, Gilewski A, Newson M, Jones H, Glowacki B A and Klamut J, "Pulsed transport critical currents of Bi2212 tapes in pulsed magnetic fields", *Supercon. Sci. Technol.* **15** 1151-1155, 2002

[64] Rondeaux F, Bredy Ph and Rey J M, "Thermal conductivity measurements of epoxy systems at low temperature" *CRC Press* 12-136, 1993

[65] Rosseinsky M J and Prassides K, "Material science: Hydrocarbon superconductors" *Nature* **464** 39-41, 2010

[66] Schwarz M, Weiss K P, Heller R, and Fietz W H, "Thermal conductivity measurement of BSCCO tapes for current lead applications" *Adv. Cryogenic Eng. Mater.* **54** 445, 2008 doi:10.1063/1.2900381

[67] Seeber B, "Handbook of applied superconductivity", *Institute of Physics Publishing*, Bristol, 1998

[68] Sladek R J, "Thermal conductivity of Indium-Thallium Alloys at Low Temperatures" *Phys. Rev.* **97** 902-915, 1955

[69] Sohn M H, Kim S W, Baik S K, Jo Y S, Seo M G, Lee E Y and Kwon Y K, "Joint Resistances Between Two Paraller High Tc Superconducting Tapes" *IEEE Trans. Appl. Supercond.* **13** 1764-1767, 2003

[70] Stenvall A, Korpela A, Mikkonen R and G Grasso, "Stability considerations of multifilamentary MgB_2 tape" *Supercond. Sci. Technol.* **19** 184-189, 2005.

[71] Stenvall A, Korpela A, Lehtonen J and Mikkonen R, "Two ways to model voltage-current curves of adiabatic MgB_2 wires" *Supercond. Sci. Technol.* **20** 859-864, 2007.

[72] Stenvall A, Hiltunen I, Korpela A, Lehtonen J, Mikkonen R, Viljamaa J and Grasso G, "A checklist for designers of cryogen-free MgB_2 coils" *Supercond. Sci. Technol.* **20** 386-391, 2007.

[73] Stenvall A, Hiltunen I, Järvelä J, Korpela A, Lehtonen J and Mikkonen R, "The effect of sample holder and current ramp rate on a conduction-cooled $V-I$ measurements of MgB_2." *Supercon. Sci. Technol.* **21** 065012, 2008

[74] Stenvall A, Mikkonen R and Kováč P, "Relation between transverse and longitudinal normal zone propagation velocities in impregnated MgB_2 windings" *IEEE Trans. Appl. Supercond.* **19** 2403-2406, 2009.

[75] Swenson C A, "Properties of Indium and Thallium at Low Temperatures " *Phys. Rev.* **100** 1607-1614, 1955

[76] Vase P, Flükiger R, Leghissa M and Glowacki B, "Current Status of High-T_c wire" *Supercon. Sci. Technol.* **13** R71-R84, 2000

[77] Vinod K, Abhilash Kumar R G and Syamaprasad U, "Prospects of MgB_2 superconductors for magnet applications" *Supercond. Sci. Technol.* **20** R1-R13, 2007

[78] Vysotsky V, Rakhmanov A and Ilyin Y *Physica C* **401** 57, 2004

[79] Wang Y, Lu Y, Xiao L, Lin L, Xu X and Dai S, "Index number (n) measurements on BSCCO tapes using a contact-free method", *Supercon. Sci. Technol.* **16** 628-631, 2003.

[80] Yang S et al., "Thermal conductivity and contact conductance of BSCCO-2212 material" *IEEE Trans. Appl. Supercond.* **5** 1471, 1995